https://doi.org/10.5194/egusphere-2026-4860
Preprint. Discussion started: 20 August 2026
© Author(s) 2026. CC BY 4.0 License.

The dynamical lifecycle of tropical cyclones from the perspective of potential vorticity structure

Emmanouil Flaounas[1,2], Suzanne L. Gray[3]

[1]Institute for Atmospheric and Climate Science, ETH Zurich, Zurich, Switzerland
[2]Institute of Oceanography, Hellenic Centre for Marine Research, Athens, Greece
[3]Department of Meteorology, University of Reading, Reading, UK

Correspondence to: Emmanouil Flaounas (em.flaounas@hcmr.gr)

Abstract. Although intense tropical cyclones (TCs) are widely associated with a potential vorticity (PV) tower, the relative contributions of diabatic and frictional processes to their evolving PV structure remain poorly quantified. Conceptualising TCs as meso-scale PV anomalies, we use online model diagnostics to decompose the PV budget into diabatic and frictional components, revealing how these processes generate the evolving PV structure that controls tropical cyclone intensification, maintenance and decay. TCs Katrina (2005) and Usagi (2013) serve as exemplary cases to identify common dynamical mechanisms governing PV evolution across TC life cycles. During TC intensification, convection acts as the main source of PV production, thereby driving TC development and intensification with the characteristic cloudless eye of TCs gradually becoming a spatially distinct substructure. A previously unknown dynamical balance emerges in the lower eye between negative PV generated by longwave radiative processes at the ocean surface, which is advected into the eye, and positive PV generated by the interaction of frictional processes with the strengthening eyewall baroclinic zone. The two contrasting contributions are large in absolute PV value, with the positive PV generated by frictional forces outweighing the negative PV contribution from longwave radiation. PV inversion diagnostics performed using a novel machine learning approach suggest a relatively weak net contribution of these contrasting processes to the cyclone's maximum intensity of ~10–15%. The PV within the upper part of the TC eye is dominated by positive contributions to the PV budget from diabatic processes and frictional forces, with the latter also contributing an additional 10-15% to the maximum intensity of TCs. Within the eyewall, latent heat release retains its positive feedback on TC intensification throughout the TC life cycle, with surface sensible and turbulent heat fluxes either counterbalancing or enhancing this positive feedback depending on altitude. Finally, we show that the spatial structure of PV plays a paramount role in the intensification and maintenance of a TC. TC decay commences

https://doi.org/10.5194/egusphere-2026-4860
Preprint. Discussion started: 20 August 2026
© Author(s) 2026. CC BY 4.0 License.

when this structure can no longer be sustained owing to the accumulation of negative PV within the cyclone eye due to longwave radiation, highlighting ocean surface processes as critical to the cyclone's life cycle.

1 Introduction

Further understanding of the complex processes that lead to the development of tropical cyclones (TC) is of paramount importance for building more solid foundations in the advancement of high-impact weather forecasting (e.g. Mogensen et al., 2017) and in the quantification of future environmental risks in a changing climate (Emanuel, 2005; Bhatia et al., 2018). The complex interactions between oceanic and atmospheric processes including latent heat release, wind shear, surface fluxes, and convective organisation are proposed to govern the formation, intensification, and decay of TCs. In these regards, different paradigms have emerged to explain the underlying dynamics of TC development with the most renowned one being the Wind-Induced Surface Heat Exchange (WISHE) paradigm and more lately the Rotating Convection paradigm. The WISHE paradigm has been formulated in an axisymmetric framework where a positive feedback mechanism links surface wind intensification and enhanced enthalpy fluxes from the ocean (Emanuel, 1986). In contrast, the rotating convection paradigm posits that localised, deep convective bursts in a rotating environment can aggregate cyclonic vorticity and lead to system-scale organisation (Montgomery and Smith, 2014); this perspective places greater emphasis on mesoscale convective processes, vertical vorticity stretching, and vortex merger compared to WISHE. A process-wise potential vorticity (PV) budget perspective on the intensification mechanism of TCs is missing from these paradigms, despite its usefulness in interpreting the origin and role of different processes in extratropical cyclone development (Wernli and Gray, 2024). Rather than proposing a new paradigm, in this study we aim to contribute to the understanding of TC development by delineating their distinct life stages and substructures from the perspective of diabatic processes and frictional forces that largely define the PV budget in the tropics.

Here we define cyclone dynamics as the interactive scheme of different atmospheric processes that result in sustaining or changing the cyclonic circulation of the wind around cyclone centres. In this context, the conceptualisation of PV as a single variable that incorporates the whole atmospheric state was a milestone for modern meteorology (Rossby, 1937). PV provides a direct relationship between the different (thermo-)dynamical processes and the development of cyclonic circulation (see Methods). Consequently, it is an excellent diagnostic

https://doi.org/10.5194/egusphere-2026-4860
Preprint. Discussion started: 20 August 2026
© Author(s) 2026. CC BY 4.0 License.

for cyclone dynamics: any cohesive mesoscale PV anomaly in an area of low stratification such as the troposphere may be inverted to yield the circulation of a cyclone system (invertibility trait). Indeed, cyclone systems, especially TCs, correspond to structurally, well-defined, localised positive PV anomalies (Montgomery et al., 2006; Campa and Wernli, 2013). Being a conserved variable under adiabatic and frictionless conditions, PV acts as an atmospheric tracer (tracer trait). However, in realistic atmospheric conditions, air masses are constantly exchanging temperature and momentum with their environment. Therefore, PV is not conserved and thus quantifying the relative contribution of different atmospheric processes to the atmospheric budget of PV is equivalent to quantifying the role of these processes in cyclone dynamics (Davis and Emanuel, 1991; Stoeligna, 1996; Zhang and Kieu, 2005; Flaounas et al., 2021).

As a diagnostic variable, PV has been extensively used to understand TC dynamics in the past (Molinari et al., 1998; Wu and Wang, 2000; Agusti-Panareda et al., 2004, 2005; Röbcke et al., 2004; Martinez et al., 2019). For instance, stratospheric air intrusions in lower latitudes due to Rossby wave breaking have been shown to impose high PV anomalies and trigger cyclogenesis through baroclinic instability (Hoskins et al., 1985). In another example on tropical cyclogenesis, the development of TC Chris (2002) has been attributed to the aggregation of nearby PV anomalies into a single “upright central monolithic PV core” (Tory et al., 2006). In these examples, it is the tracer trait of PV that enables backtracking the formation of cyclone systems to their environmental forcing. On the other hand, piecewise PV inversion has been crucial to quantify the role of different cyclone substructures in cyclone development (Davis et al., 1992). For instance, Shapiro and Möller (2003) isolated and solely inverted the PV in the upper troposphere to quantify and show the important relative contribution of an upper-level trough to the development of TC Opal (1995). Similarly, Kieu and Zhang (2010) developed a piecewise PV inversion method to quantify the relative contribution of specific substructures (i.e. PV anomalies within the cyclone system) such as the eye and convective eyewall to the intensity and warm-core formation of an idealised TC. More recently Shi and Chen (2021) used similar methods to show that PV due to diabatic heating is driving the rapid intensification of Supertyphoon Lekima (2019). Finally, Murthy and Boos (2019) used a PV-budget diagnostic analysis to show the distinct role of moist convective heating and adiabatic advection to jointly shape the vertical structures of PV towers in tropical depressions. More than understanding the role of specific PV anomalies in cyclone dynamics, the combination of PV-thinking and atmospheric modelling provides an exceptionally useful framework to quantify the role of specific atmospheric processes therein.

https://doi.org/10.5194/egusphere-2026-4860
Preprint. Discussion started: 20 August 2026
© Author(s) 2026. CC BY 4.0 License.

Indeed, the delineation of the PV partition due to diabatic and momentum-forcing to the atmospheric state provides the means to calculate a process-based PV budget (see Methods) but, more than that, it provides the means to employ piecewise PV inversion for the ends of quantifying the relative contribution of different processes to the formation of cyclone systems. To our knowledge, such a framework has been only applied to extratropical and Arctic cyclones (Stoeligna, 1996; Bracegirdle and Gray, 2009; Chagnon et al., 2013; Croad et al., 2023). Stoeligna (1996) was the first to use atmospheric modelling for the ends of quantifying the dominant contribution of convection to the development of an extratropical cyclone, when compared to its baroclinic forcing. In a similar approach, Flaounas et al. (2021) simulated 100 cases of Mediterranean cyclones and demonstrated a continuum range of relative contribution of baroclinic and diabatic forcing to the development of these systems. Undoubtedly, the use of PV-thinking and piecewise PV inversion have been excellent diagnostic approaches in the field of cyclone dynamics. However, to our knowledge, their application to TCs has been especially limited compared to their broader use in the analysis of extratropical systems, especially concerning the quantification and piecewise inversion of process-wise PV budget components.

From the perspective of atmospheric processes, the deep convective eyewall and the high underlying sea surface temperature (SST) of TCs suggest an exceptional production of diabatic PV due to latent heat (e.g. Jones et al., 2003; Hendricks et al., 2004; Nguyen et al., 2011; Martinez et al., 2019). This source of PV could dominate the entire PV budget in TC centres and thus function as the sole modulator of cyclone intensity. On the other hand, TC warm cores form a circular frontal zone of intense radial temperature gradients that dynamically separate the eye from its colder surroundings. Such a baroclinic zone could interact with frictional forces and result in a net PV production close to the centre of TCs. Indeed, for extratropical cyclones Davis et al. (1993) and Stoelinga (1996) used PV inversion and showed that frictional forces may interact with horizontal baroclinicity along mid-latitude fronts and lead to the net production of PV within the lower atmospheric levels (see Methods). More recently, Adamson et al. (2006) showed that such PV production may be transferred through advection and affect dynamically remote areas to cyclone centre. Despite their potential importance, frictional forces correspond to a largely overlooked process which could have an ambiguous feedback to cyclone intensity and consequently be strongly involved in cyclone dynamics. For instance, Attinger et al. (2022) used process-wise PV budget and found a small fraction of extratropical cyclones for which most of the PV in their centres was due to frictionally produced PV. Similarly, Flaounas et al. (2021) used an exemplary Mediterranean cyclone case to demonstrate that frictionally produced PV can be concentrated into cyclone centres, dominate the PV budget therein and thus

https://doi.org/10.5194/egusphere-2026-4860
Preprint. Discussion started: 20 August 2026
© Author(s) 2026. CC BY 4.0 License.

define the cyclonic circulation. How high-valued is such frictionally-produced PV in TCs, what is its potential role in TC dynamics and which processes contribute to baroclinicity between their warm-core and colder surroundings are all open questions. Finally, it is rather unclear how diabatic forcing due to longwave radiation and turbulent heat fluxes might affect the total PV budget and what is its consequent impact on TC dynamics.

Insights into TC dynamics from a process-based PV analysis is indeed missing from the state-of-the-art. It is thus in this context that we employ high-resolution atmospheric modelling for the ends of analysing the dynamics of two well known, intense and destructive TCs of the recent past: Katrina (2005) and Usagi (2013). Both TCs rapidly developed into especially intense cyclone systems making landfall in inhabited areas of US and China, respectively, while producing substantial socioeconomic impacts. In particular our twofold objective depends on the derivation of a process-based PV budget, aiming to identify different dynamical substructures and processes that majorly contribute to TCs development and use these results to propose distinct phases of TC development from the perspective of PV. Both the organisation and discussion of our results rely on the mathematical terms of PV tendency equations, which are explicitly discussed and presented in the following section.

2. Methods

2.1 Model simulations

We used the WRF model V4.4.2 (Skamarock et al. 2019) to simulate TCs Katrina (2005) and Usagi (2013) in a moving nest framework with two domains (Gopalakrishnan et al. 2006). The parent domain derived its initial and boundary conditions from three-hourly fields of the 5th generation reanalysis from the European Centre for Medium-Range Weather Forecasts (ERA5; Hersbach et al., 2020) at a grid spacing of 0.25 degrees in longitude and latitude. The SST is also taken from ERA5 and is updated in both domains every hour. A parent domain encompasses the whole track of Usagi and a nested square domain of 1,500 km per side always follows the cyclone centre. The displacements of the nested domain are predefined, according to the cyclone tracks as diagnosed from ERA5, which are consistent with the observed ones from International Best Track Archive for Climate Stewardship (IBTrACS, Knapp et al., 2010; Fig. 1). For Usagi, the simulation initial conditions for both domains were set on 15 September 2013, 1600 UTC and the model integration ended on 22 September 2013, 2300 UTC; for Katrina the corresponding times are 23 August 2005, 1800 UTC and 31 August 2005, 1100 UTC.

https://doi.org/10.5194/egusphere-2026-4860
Preprint. Discussion started: 20 August 2026
© Author(s) 2026. CC BY 4.0 License.

In both simulations, the model integration in the parent domain was performed using a horizontal grid spacing of 7.5 km and a time step of 30 s; for the inner nested domain the spacing was 2.5 km and timestep 10 s. For both domains, we used 101 vertical levels up to the model top at 50 hPa with the first model level being fixed at 10 m above the surface. Vertical levels follow topography at lower atmospheric levels and eventually align with pressure levels in the upper levels. To ensure that the simulated tracks would not significantly diverge from those in ERA5, the wind, temperature, and water vapour fields in the parent domain were nudged at every grid point toward ERA5 with coefficients of 0.001, 0.001, and 0.0001 s^{-1}, respectively. This framework ensured consistent simulated cyclone tracks and life stages with ERA5. The nested domain was free to resolve cyclone dynamics at high resolution. Parameterizations used include the Purdue Lin Scheme for microphysics (Chen and Sun, 2002), the Yonsei University Scheme (YSU) for the planetary boundary layer (Hong et al., 2006), the Revised MM5 Scheme for the surface layer (Jimenez et al., 2012), the RRTMG scheme for longwave and shortwave radiation (Iacono et al., 2008), and the Unified Noah Land Surface Model (Tewari et al., 2004). The New Tiedtke convection Scheme (Zhang and Wang, 2017) was applied only to the parent domain.

When compared with IBTrACS and ERA5, the model simulations reproduced the cyclone tracks and intensities reasonably realistically (Fig. 1). For Usagi, the simulated track shows a nearly constant westward displacement of about 67 km along the entire trajectory relative to both IBTrACS and ERA5 (Fig. 1a). The minimum MSLP, used here as a measure of cyclone intensity, is reproduced quite accurately and reached at the same time as in IBTrACKS (Fig. 1b); however, the intensification phase (defined by rapid deepening) begins about 12 hours earlier than indicated by IBTrACS, albeit with a similar deepening rate, resulting in MSLP dropping from around 1000 hPa at 0000 UTC on 16 September 2013 to about 910 hPa at 1800 UTC on 19 September 2013. Thereafter, both WRF and IBTrACS show a weaker MSLP increasing rate, indicating a comparable evolution during the later stages. For Katrina, the track is reproduced more accurately (Fig. 1c), and the evolution of intensity is also realistic (Fig. 1d), although the minimum MSLP is reached with a time lag of about 15 hours relative to IBTrACS and is shallower by about 10 hPa (only the NOAA track is available for Katrina in IBTrACS). Despite the differences in track position and timing of intensification, the TC track and MSLP deepening rates are overall realistically reproduced by the model. Therefore, we consider the simulations to be an adequate basis for studying cyclone development from a PV perspective.

https://doi.org/10.5194/egusphere-2026-4860
Preprint. Discussion started: 20 August 2026
© Author(s) 2026. CC BY 4.0 License.

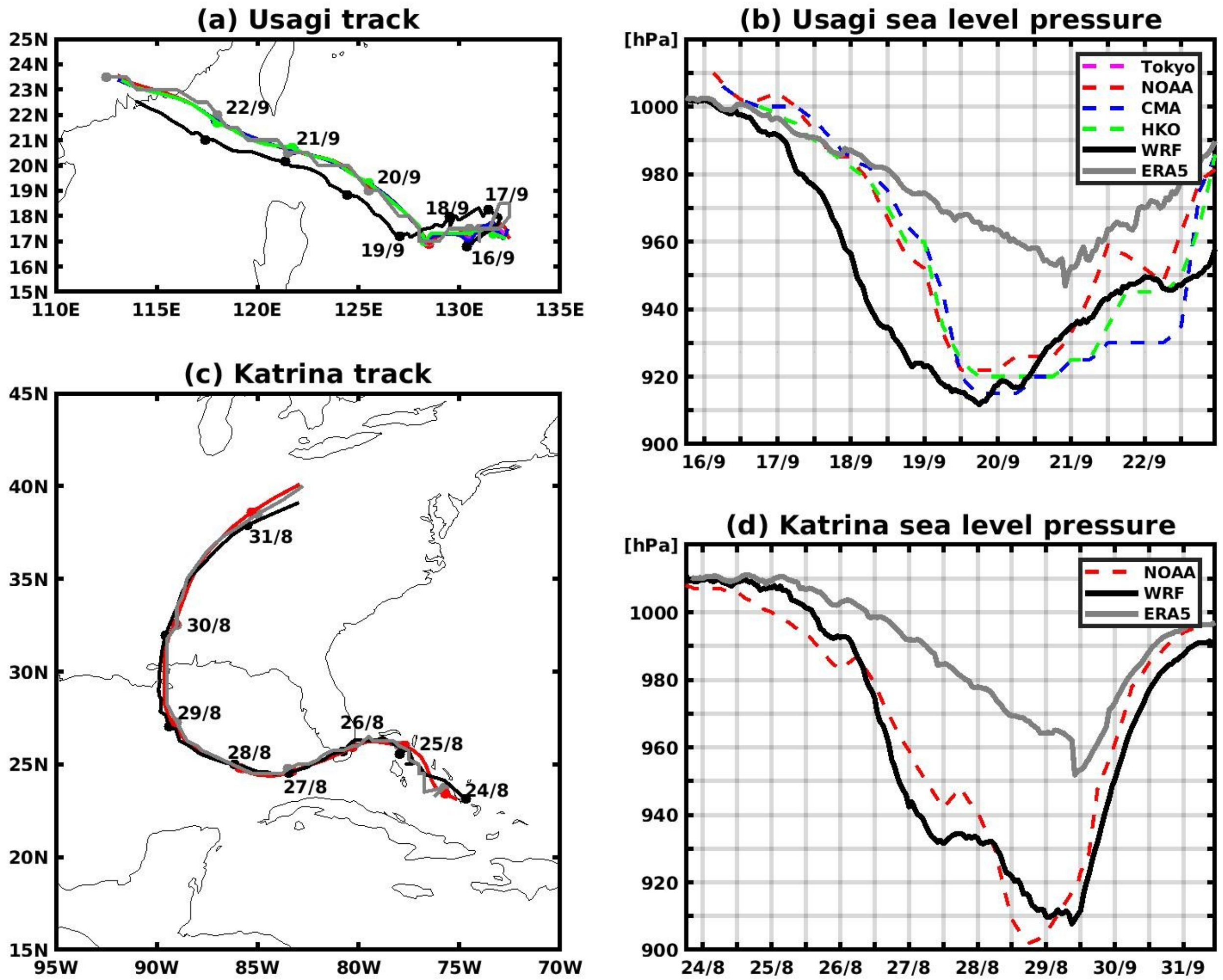

Figure 1: Tracks and MSLP evolution for Usagi and Katrina. (a) Cyclone tracks of TC Usagi from IBTrACKS, ERA5 and the WRF simulation (legend in Fig. 1b). (b) Time evolution of minimum MSLP in TC Usagi's centre from the WRF simulation (black lines), from IBTrACKS (dashed lines) and ERA5 (grey line). (c) and (d), as in (a) and (b) but for TC Katrina.

2.2 PV and diabatic tracer diagnostics

PV has been defined by Ertel (1942) as

$$q = \frac{\zeta \cdot \nabla \theta}{\rho}, \qquad \text{Eq. 1}$$

https://doi.org/10.5194/egusphere-2026-4860
Preprint. Discussion started: 20 August 2026
© Author(s) 2026. CC BY 4.0 License.

where ρ is the air density, $\boldsymbol{\zeta}$ is the absolute vorticity and θ is the potential temperature. As discussed in the introduction, PV is a conserved variable under adiabatic and frictionless atmospheric conditions. Therefore, material changes in PV may be quantified according to

$$\frac{Dq}{Dt} = \frac{1}{\rho}\left(\boldsymbol{\zeta} \cdot \nabla \dot{\theta} + \nabla \times \boldsymbol{F} \cdot \nabla \theta\right), \qquad \text{Eq. 2}$$

where $\dot{\theta}$ is the time derivative of θ (equivalent to the diabatic forcing) and $\boldsymbol{F}$ is a mixed term that includes all momentum forcing to an air parcel and so both surface frictional forces and turbulence. To quantify the origin of total atmospheric PV, we implemented a diagnostic module into the WRF model that was first presented and used in Flaounas et al. (2021). This module calculates a process-based PV budget at every model time-step by decomposing total atmospheric PV into three additive components (hereafter referred to as PV-tracers). The first PV-tracer concerns the conserved part of PV (PV_{co}). This PV-tracer is equal to the total PV at the model initial conditions and is updated at every model time step at the model boundary conditions where it is set equal to the total atmospheric PV. Therefore, PV_{co} represents the total atmospheric PV that pre-existed the cyclone occurrence or the total atmospheric PV that is introduced into the model domain through the model boundaries. Our PV budget diagnostic operates independently in each model domain. Therefore, in a relatively small, nested domain (i.e. square domain of 1500 km per side), one may interpret PV_{co} as the external, environmental influence on the resolved cyclone dynamics.

In addition to PV_{co}, we introduce two main non-conserved PV tracers. The first represents the diabatic forcing of cyclone dynamics (PV_{diab}). This PV tracer includes the sum of temperature tendencies from microphysics, radiation, and planetary boundary layer (PBL) parameterizations (i.e., the first term on the right-hand side of Eq. 2). PBL parameterization is calculating momentum and temperature tendencies throughout the atmospheric column due to vertical sub-grid-scale fluxes from eddy transports. In contrast to PV_{co}, this tracer is zero in the model's initial and boundary conditions, but it is continuously updated at every model time step and at every grid point within the domain according to the right-hand side of Eq. 2. The second non-conserved PV tracer represents the momentum forcing of cyclone dynamics (PV_{mo}). This tracer includes momentum tendencies derived solely from the PBL parameterization (i.e., $\boldsymbol{F}$ in the second term on the right-hand side of Eq. 2). PV_{diab} is further broken down to different PV-tracers, one per temperature tendency from individual parameterizations: PV_{mp} for

https://doi.org/10.5194/egusphere-2026-4860
Preprint. Discussion started: 20 August 2026
© Author(s) 2026. CC BY 4.0 License.

microphysics, PV_{bl} for PBL, PV_{lw} for longwave radiation, and PV_{sw} for shortwave radiation. All PV-tracers are updated and subject to advection during all model time steps according to

$$q_x(\tau)=q_x(0)+\int_1^{\tau} -\boldsymbol{v}\cdot\nabla q_x+G_x\,dt, \qquad \text{Eq. 3}$$

$$G_x=\frac{1}{\rho}\left(\boldsymbol{\zeta}\cdot\nabla T_x\right)$$
$$G_{(x=mo)}=\frac{1}{\rho}\left(\nabla\times\boldsymbol{F}\cdot\nabla\theta\right). \qquad \text{Eq. 4}$$

Here, $\boldsymbol{v}$ represents the three-dimensional wind field, while q_x and T_x denote a PV tracer and a parameterization temperature tendency, respectively, at a given time step τ, associated with process *x* (*co*, *mp*, *cu*, *bl*, *sw*, *lw*, or *mo*). The term $q_x(0)$ refers to the value of the PV tracers in the model's initial conditions, whereas PV sources and sinks are represented by G_x. Ideally, at any model time step, the sum of all PV tracers should equal the total atmospheric PV:

$$q=q_{co}+q_{diab}+q_{mo}+q_r. \qquad \text{Eq. 5}$$

q_r denotes the residual of the budget, whereas ideally q_{diab} can be still decomposed to q_{mp}, q_{sw}, q_{lw} and q_{bl}. Similarly to PV-tracers, θ has also been treated as a tracer (θ-tracers hereafter), being subject to advection and to accumulations of temperature tendencies from parametrisations. Consequently, we have defined one conserved (θ_{co}), one non-conserved (θ_{diab}) and several θ-tracers stemming from each parametrisation output (i.e., θ_{mp} for microphysics, θ_{bl} for PBL, θ_{lw} for longwave radiation and θ_{sw} for shortwave radiation) where

$$\theta=\theta_{co}+\theta_{diab}+\theta_r. \qquad \text{Eq. 6}$$

The term G_x in Eq. 4 is calculated following Flaounas et al. (2021). However, in this study, the tracers are not introduced as scalars; instead, they mimic the model prognostic equation for θ. Consequently, advection does not use the average wind tendency from the acoustic steps during the Runge–Kutta time integration scheme of the dynamical core, but rather occurs gradually, as in the model prognostic equations for θ. Sensitivity tests showed

https://doi.org/10.5194/egusphere-2026-4860
Preprint. Discussion started: 20 August 2026
© Author(s) 2026. CC BY 4.0 License.

that this implementation yields higher precision compared to that of Flaounas et al. (2021). Indeed, this approach yields an insignificantly small θ_r, several orders of magnitude lower than the smallest θ-tracer. On the other hand, PV-tracers might reach relatively high values in specific substructures of the cyclone system. While we use the same approach as for the θ-tracers, PV depends on spatial gradients of parametrization tendencies (Eq. 4), which might reach especially large values in high-resolution simulations. For high resolution simulations such as the ones used here, we used sixth-order centred finite differences on the staggered grid for the horizontal gradients and first-order centred finite differences on the vertical staggered grid. As discussed below, PV-tracers tend to cancel each other, but given the sharp gradients of temperature tendencies and the high wind speeds within TCs, even comparably small errors in the PV-budget would still yield relatively high q_r, as they will be accumulating at every time step. The appendix shows q_r for three selected times at the stages of intensification, maturity, and decay (these times are further discussed in the next section). For the cyclone system, the magnitude of q_r has been found to be smaller for Usagi than for Katrina, but for both cases, the PV-tracers' amplitude does not hinder a clear interpretation of how specific processes contribute to TC dynamical structure. Therefore, in the rest of the document, we use the PV-tracers for the interpretation of the role of specific atmospheric processes in the dynamical structure of TCs rather for an accurate quantification of the PV budget.

2.3 Neural-network-based PV inversion

We trained an ensemble of U-Net convolutional neural networks to perform axisymmetric PV inversion. The networks were trained using outputs from a large ensemble of two-dimensional idealised tropical cyclone simulations generated with the Cloud Model 1 (CM1; Bryan, 2012, 2021). Across the simulations, different combinations of coefficients were applied to systematically amplify or suppress specific parameterised temperature tendencies. In addition, separate experiments set all parameterised tendencies to zero either in the lower or upper half of the vertical domain. These simulations were designed to generate a wide range of physically consistent vortex structures, thereby providing a diverse and representative training dataset at same horizontal resolution to that of the WRF nested domains (2.5 km). Model outputs of PV, θ, and tangential wind fields were interpolated onto a common pressure grid.

The training procedure comprises several U-Net–type architectures that map a two-dimensional PV field (in radius–pressure space) to the corresponding balanced tangential wind and thermodynamic structure. We used two variants: a baseline U-Net with dilated residual bottleneck layers, and a more parameter-efficient version

https://doi.org/10.5194/egusphere-2026-4860
Preprint. Discussion started: 20 August 2026
© Author(s) 2026. CC BY 4.0 License.

incorporating depthwise-separable convolutions and channel-attention mechanisms. Training minimises a composite loss that combines supervised reconstruction error with a physics-based consistency constraint, enforcing that the PV diagnosed from the predicted fields matches the input PV. A two-stage training strategy is used to optimise U-Net performance in piecewise PV inversion (Davis, 1992). In this context, we aimed to enforce physically meaningful linearity in piecewise PV inversion. For this reason, selected models were further trained after completing 80-epoch cycle of learning full PV inversion. Additional training included PV decomposition constraints based on amplitude, sign, and vertical splits, requiring from U-net a consistency between the inversion of full and partitioned PV fields. In total, an ensemble of 13 network configurations were used for piecewise PV inversion. Details on the simulations, preprocessing, architectures, training procedure, and validation are provided in the supplement.

3. Results

3.1 Dynamical lifecycle of TC Usagi and Katrina under the prism of conserved and non-conserved processes

Figures 2a and 2b show the Hovmöller diagrams of total atmospheric PV, averaged within a 100 km radius around the TC centres. Given that PV_{co} presents negligibly low values within the troposphere and the residual is rather small in such averaging, the total atmospheric PV in Figs. 2a and 2b is largely defined by the sum of PV_{diab} and PV_{mo}. Therefore, the other Hovmöller diagrams in Fig. 2 only show these two non-conserved components. Finally, to ease comparison of PV budget with cyclone intensity, Figs. 2g and 2h show the temporal evolution of MSLP at the TC centres (as also shown in Fig. 1). Three specific times are selected for analysis (here and in later figures) and marked by vertical lines in the panels: (1) the development stage, when the MSLP presents a strong deepening rate and the negative PV_{diab} starts building its bottom-up structure; (2) the mature stage, when MSLP reaches to its minimum; and (3) the decay stage, when MSLP is increasing while the cyclone intensity is weakening.

For both cyclones, Figs 2a and 2b show similar amplitudes of PV values and comparable vertical profiles. Indeed, from the earliest times of Fig. 2, both average PV profiles typically exceed 1 PVU (yellow shading), suggesting the formation of relatively homogeneous PV towers close to the cyclone centre, vertically extending from the surface to the tropopause. The (dynamical) tropopause is defined by the 2-PVU surface first reached on descending from the top of the domain shown (with the high PV values above the tropopause indicating

https://doi.org/10.5194/egusphere-2026-4860
Preprint. Discussion started: 20 August 2026
© Author(s) 2026. CC BY 4.0 License.

stratospheric air). While the cyclones evolve, higher PV values begin to appear in the mid-troposphere, between 5 and 12 km of altitude (dashed lines in Figs. 2a and 2b). As discussed in the next section, this layer corresponds to the region of maximum snow concentration, with the melting level roughly located near 5 km right below an increasing concentration of cloud mixing ratio with height. Thereafter, at the time of maturity (t_0), when the cyclone reaches its maximum intensity (minimum MSLP; Figs. 2g, h), the vertically averaged PV within the core also reaches its maximum, extending from the surface to approximately 12 km altitude. Such a temporal alignment is expected because the mature cyclone exhibits its strongest cyclonic vorticity and together with important θ anomalies, it also produces the largest positive PV anomalies. Owing to the invertibility property of PV, these enhanced PV anomalies are intrinsically linked to the cyclone circulation, highlighting the importance of understanding the processes that govern PV evolution and, consequently, cyclone development. For this reason, Figs 2c and 2d show Hovmöller diagrams of PV_{diab} and Figs 2e and 2f show these for PV_{mo}.

For both cyclones, the non-conserved components show similar structural and temporal evolution. In particular, Figs 2c and 2d show a striking vertical discontinuity of PV_{diab}, where negative values begin a bottom-up development at t_{0-43h} for Usagi and at t_{0-63h} for Katrina. Interestingly, for both cyclones, these times coincide with PV values first exceeding 2 PVU in the mid-tropospheric layer between 5 and 12 km (in Figs 2a and 2b), as well as the steepest deepening rates of MSLP (Figs 2g and 2h), signalling the time of maximum intensification of the TCs. At maturity (t_0), negative PV_{diab} values close to the surface reach to an altitude of about 1 km for Usagi and up to 3 km for Katrina. These negative values are vertically followed by positive values up to around 15 km altitude, and then by negative values again with their minimum being close to 18 km of altitude. In fact, PV_{diab} and PV_{mo} show contrasting contributions to cyclone development, with PV_{mo} always counteracting the negative feedback of PV_{diab} to the PV budget. As a result, the sum of PV_{diab} and PV_{mo} leads to an overall positive PV budget in the lower and upper troposphere. It is however noteworthy that PV_{mo} and PV_{diab} in Katrina both abruptly change sign close to the surface after t_{0+10h}. In fact, this timing coincides with the cyclone's landfall, suggesting that the change of sign may be linked to the influence of surface changes on the cyclone system. Up to that point, however, both TCs exhibit similar structures of the two non-conserved PV components in Fig. 2.

PV_{mo} always yields positive values throughout the atmospheric column with higher values close to the surface, except Katrina after making landfall. This finding indicates an important positive contribution of momentum-

https://doi.org/10.5194/egusphere-2026-4860
Preprint. Discussion started: 20 August 2026
© Author(s) 2026. CC BY 4.0 License.

forcing processes to the overall PV budget due to frictional forces close to surface and turbulence in the mid and upper troposphere (variable ***F*** in Eq. 2). On the other hand, diabatic processes exert a contrasting effect on the cyclonic circulation through the negative and positive values of PV_{diab}. As a result, if we conceptualise the dynamical lifecycle of both TCs as a modulating PV anomaly, PV_{mo} contributes primarily to cyclone development close to the surface by overweighting the negative contribution of PV_{diab}, while PV_{diab} contributes primarily by playing the leading role in yielding high-valued positive PV in the mid-troposphere. Most importantly, the Hovmöller diagrams show similar structures of PV_{diab} and PV_{mo} anomalies but with opposite signs, suggesting comparable timings and interconnected processes of PV destruction and production for PV_{diab} and PV_{mo}, respectively. These interconnected processes are further analysed and discussed in subsequent sections along with the substructures and the processes that govern the dynamical lifecycle of both cyclones.

https://doi.org/10.5194/egusphere-2026-4860
Preprint. Discussion started: 20 August 2026
© Author(s) 2026. CC BY 4.0 License.

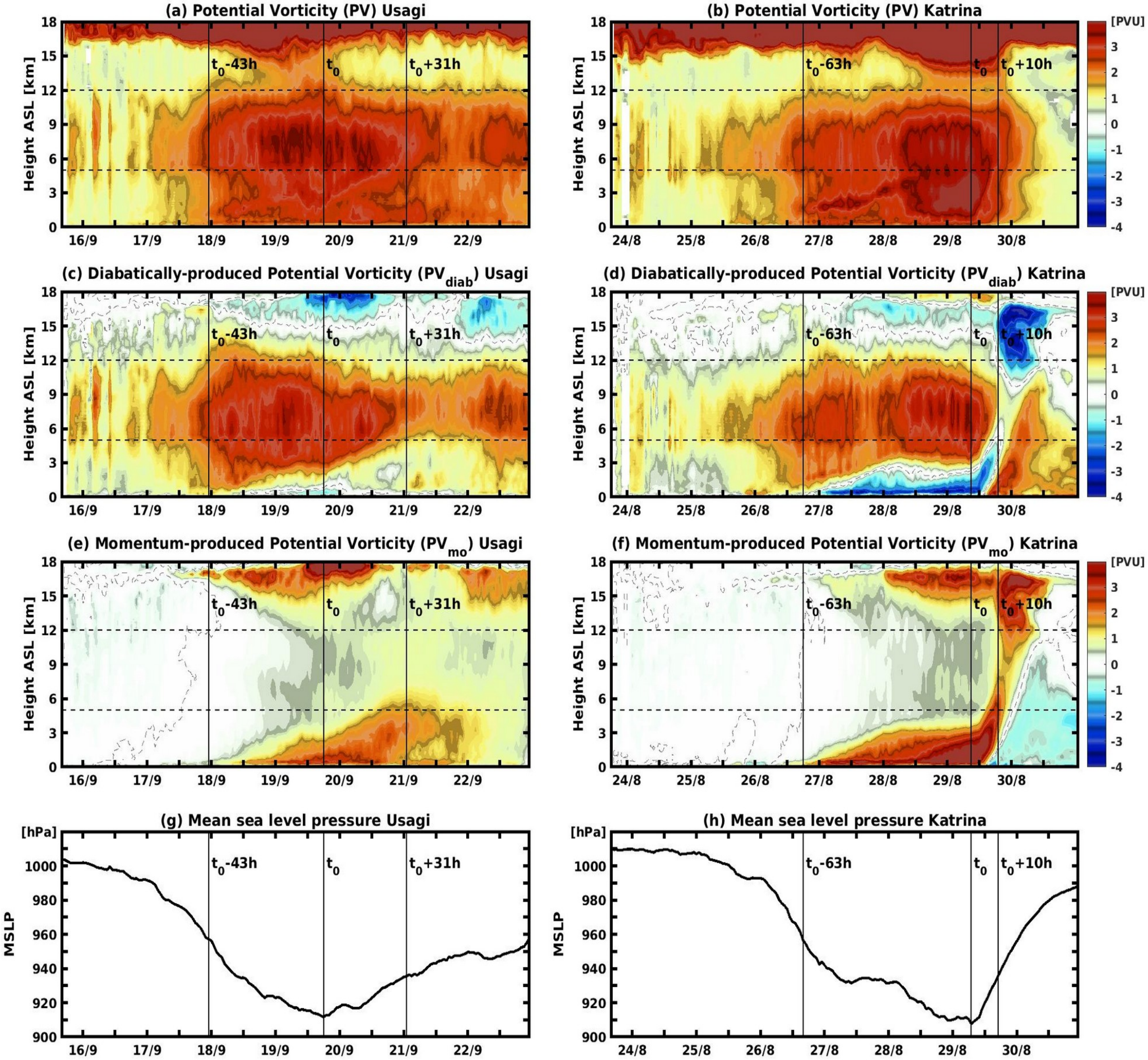

Figure 2: PV and MSLP evolution for Usagi and Katrina. (a) Hovmöller diagram of total atmospheric PV (shading) averaged within 100 km around the centre of Usagi; dashed contour depicts the isoline of 0 PVU, horizontal dashed lines depict the levels of 5 and 12 km above sea level (asl) and vertical solid lines depict different times respect to the TC's maximum intensity (t_0). (b) as in (a), but for Katrina. (c) and (d) as in (a) and (b), but for PV_{diab} (shading); (e) and (f) as in (a) and (b), but for PV_{mo}. (g) and (h) MSLP as a measure of intensity of TCs Usagi and Katrina, respectively.

https://doi.org/10.5194/egusphere-2026-4860
Preprint. Discussion started: 20 August 2026
© Author(s) 2026. CC BY 4.0 License.

3.2 Distinct dynamical PV structures within TCs

The Hovmöller diagrams in Fig. 2 provide a spatio-temporal overview of the TCs' development stages from the perspective of PV. However, the spatial averaging may obscure dynamical substructures that are important for their development. To address this issue, Fig. 3 shows the vertical–radial average profiles of total PV, PV_{diab}, and PV_{mo} at the three selected times for TC Usagi (marked by vertical lines in Fig. 2). The two TCs show similar PV profiles, and the same analysis applies to both. For this reason, here we only present the case of Usagi, while the results for Katrina are shown in supplementary material.

Development stage: At t_0–43 h (i.e., 43 hours before Usagi reaches its mature stage, top row), the maximum average tangential wind speed is approximately 50 m s^{-1} at a height of about 1 km above the ocean surface and at a radial distance of roughly 50 km from the cyclone centre (black contour in Fig. 3a). This wind maximum coincides with the lower portion of the convective eyewall (blue contours). At this stage, TC Usagi is clearly identifiable as a distinct region of high PV, bounded by an approximate threshold of ~2 PVU (green colours). Two areas with total PV exceeding 7.5 PVU are evident (orange colours): one is located near the cyclone centre around 1.5 km altitude, and the other lies between 5 and 9 km altitude near the convective eyewall. These high PV values are consistent with the Hovmöller diagram where high PV values start to develop in the mid-troposphere (first vertical line in Fig. 2a), while lower-tropospheric values remain comparatively weak. Decomposition of the total PV into its two non-conserved components (middle and right columns of Fig. 3) shows that PV_{diab} closely mirrors the total PV (Fig. 3b), indicating that diabatically generated PV dominates the PV budget. However, in the cyclone centre near the ocean surface, negative PV_{diab} values begin to emerge, offset by positive PV_{mo}. A similar compensation is also present at higher altitudes (~17 km) directly above the cyclone centre, within the eye region outlined by the convective eyewall.

Mature stage: At t_0 (middle row), the maximum tangential wind speed increases to an azimuthally averaged value of approximately 78 m s^{-1}, accompanied by an intensification of the ascent within the convective eyewall. The cyclone's eye is now a well-defined region of high total PV (Fig. 3d), with values exceeding 7.5 PVU (orange to brown colours) forming a characteristic "bowl-shaped" pattern, similar to the one discussed by Yau et al. (2004) and with comparable peak PV magnitudes. This structure results from an "inner-bulb" of comparatively lower PV values that lies within the cyclone core, extending from the centre to a radius of ~15 km

https://doi.org/10.5194/egusphere-2026-4860
Preprint. Discussion started: 20 August 2026
© Author(s) 2026. CC BY 4.0 License.

and from the surface up to ~2 km altitude. Although the PV values of this inner-bulb are lower than their surroundings, they remain substantially high (3–6 PVU) and they are therefore expected to significantly positively contribute to the cyclone's circulation. Decomposition of the PV field into its non-conserved components reveals that PV_{diab} plays a major role in shaping the total PV distribution (Figs. 3e–f): it contributes positively across most of the cyclone system, except within the inner-bulb, where extremely negative values develop. Indeed, TC maturity is characterised by strongly negative PV_{diab} values of less than –60 PVU, expanded considerably within the cyclone centre compared to the earlier development stage when negative PV_{diab} only occupied a small area (Fig. 3b). These extremely negative PV_{diab} values are offset by positive PV_{mo} contributions yielding an overall positive PV budget (Fig. 3d). Notably, PV_{mo} is positive throughout the entire cyclone eye and at all altitudes, indicating that it exerts an overall positive contribution to the cyclone intensity.

Decay stage: At t_0+31h (bottom row), the maximum tangential wind speed decreases to approximately 60 m s^{-1}, and the ascent within the eyewall also weakens. The cyclone is therefore in a weakening phase, consistent with the reduction of total PV within the eye. At this stage, the highest PV values are concentrated in a tilted vertical structure aligned with the eyewall. The total PV field is dominated by PV_{mo}, while PV_{diab} exhibits its strongest positive values only along the eyewall. Meanwhile, the bulb of negative PV_{diab} has expanded upward, now reaching altitudes of up to ~7 km. Using tangential wind speed as a measure of TC intensity, its relation to total PV (Eq. 1) becomes evident. The black contours in Fig. 3g follow the orientation of the tilted PV tower, implying that the cyclone's weakening is linked to the reduction in total PV amplitude in the eye, a reduction governed by the competing contributions of PV_{diab} and PV_{mo}.

The ambiguous role of diabatic processes in TCs' development: In all three stages, PV_{mo} consistently contributes positively to the total PV budget, whereas PV_{diab} exhibits a mixed, sometimes opposing, influence. This ambiguity makes it necessary to further decompose PV_{diab} in order to identify the specific diabatic processes responsible for shaping the TC's total PV structure. To this end, Fig. 4 presents, for t_0, the three additive components of PV_{diab} generated by parameterised microphysics (PV_{mp}), longwave radiation (PV_{lw}), and turbulent fluxes (PV_{bl}). The contribution of shortwave radiation is negligibly small and therefore omitted. Figure 4 shows that PV_{mp} produces both positive and negative values, shaping together the characteristic "bowl-shaped" pattern of total PV seen in Fig. 3d. The positive component arises primarily from latent-heat release, while negative PV_{mp} values also

https://doi.org/10.5194/egusphere-2026-4860
Preprint. Discussion started: 20 August 2026
© Author(s) 2026. CC BY 4.0 License.

develop within the cyclone's inner-bulb. These negative values are further amplified by PV_{lw}, which contributes negatively throughout the entire eye region. In contrast, PV_{bl} generally adds positively to the PV budget, although negative values emerge at the base of the convective eyewall (here defined as the lower edge of the blue contours in the right panel of Fig. 4). Overall, microphysical processes play the dominant role in the positive production of PV_{diab}, whereas all three processes (microphysics, longwave radiative heating and cooling, and turbulent heat fluxes), jointly govern the formation and maintenance of the negative PV_{diab} bulb within the cyclone's inner-core.

From the PV invertibility perspective, Figs 3 and 4 together show that different atmospheric processes make contrasting contributions to the total PV budget and can therefore exert either positive or negative feedbacks on cyclone development. Based on these patterns, we identify two key dynamical substructures within the cyclone system: the convective eyewall and the inner-core bulb of negative PV_{diab} values. It is important to note, however, that the non-conserved PV components in Figs 3 and 4 reflect the combined effects of advection and local accumulation associated with specific physical processes. Thus, these figures depict the resulting contributions of the various atmospheric processes to the cyclone's dynamics, rather than the locations where these processes were initially produced. Therefore, the next section discusses the processes leading to PV production and destruction, linking them to the distinct dynamical substructures identified within the cyclone system.

https://doi.org/10.5194/egusphere-2026-4860
Preprint. Discussion started: 20 August 2026
© Author(s) 2026. CC BY 4.0 License.

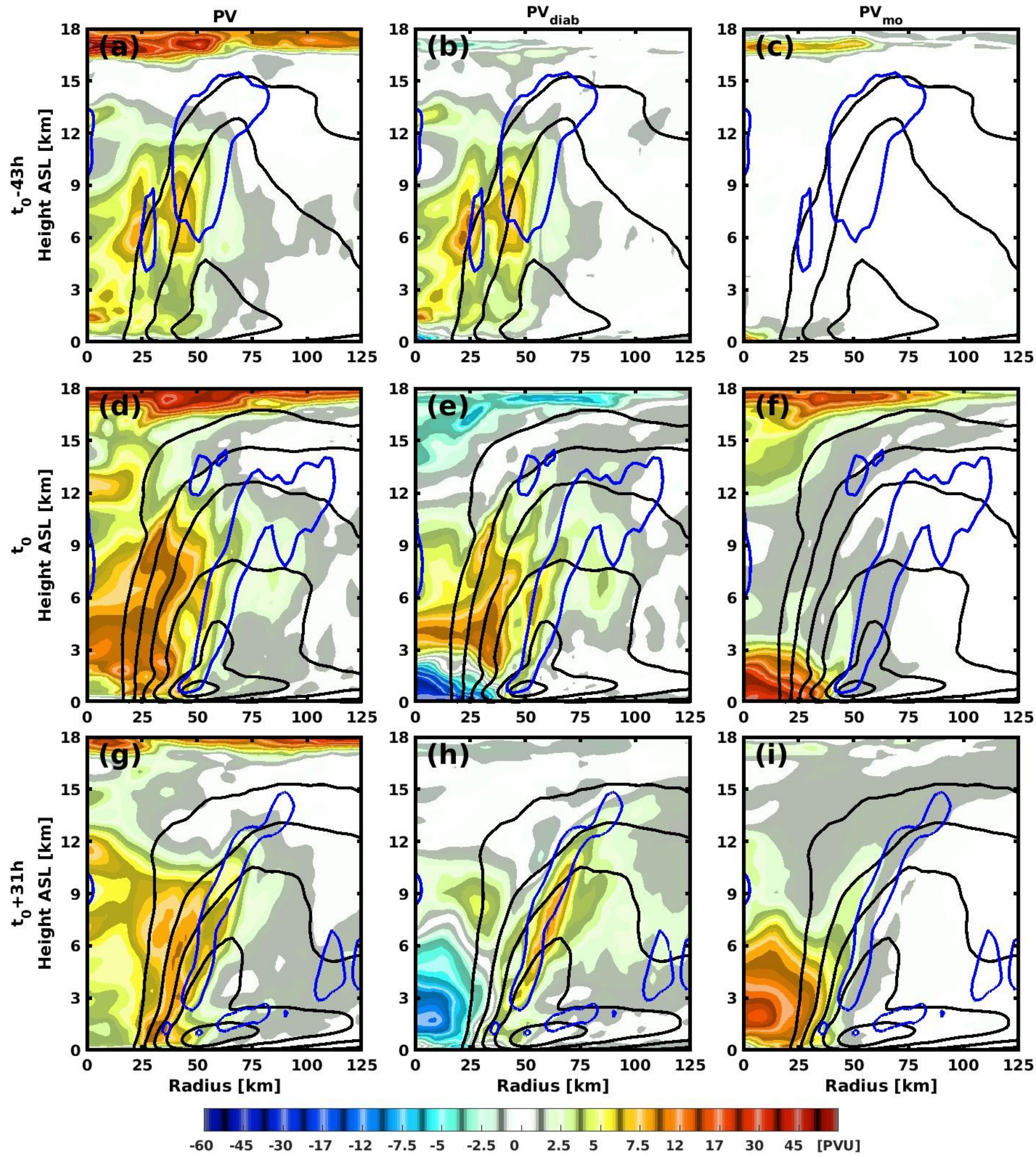

420 **Figure 3: Vertical-radial distribution of winds and PV components in TC Usagi. Colour shading is total PV, PV_{diab} and PV_{mo} in the left, middle and right columns, respectively. Each row of panels refers to different times with respect to the mature stage (t_0). Panels also show azimuthal mean tangential wind speed (in black contours every 10 m s^{-1}, starting from 20 m s^{-1}) and vertical wind speed for 0.25 m s^{-1} and 0.75 m s^{-1} (in blue contours).**

https://doi.org/10.5194/egusphere-2026-4860
Preprint. Discussion started: 20 August 2026
© Author(s) 2026. CC BY 4.0 License.

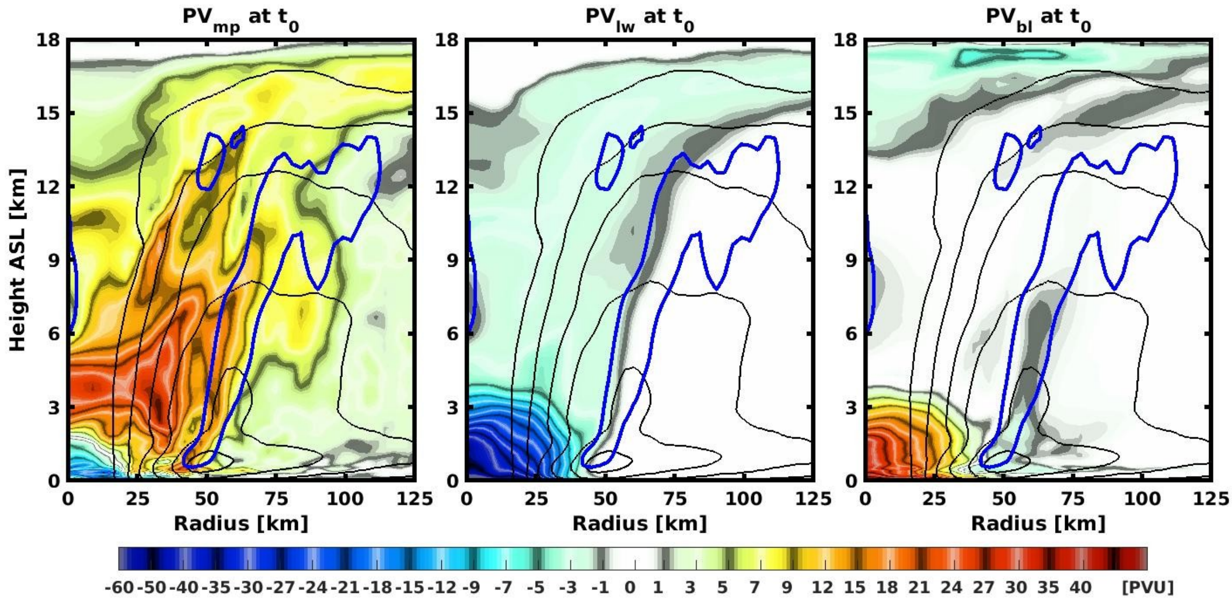

Figure 4: As for Fig. 3, but for PV_{mp}, PV_{dlw} and PV_{bl} (in colour shading) at the time of Usagi's mature stage (t_0) only.

3.3 Process-wise origin of tropical cyclone dynamical substructures

Given the tracer-trait of PV and the rapid advection of its components by the intense winds within a mature TC, it is difficult to identify from Fig. 3 the spatial origins of PV_{diab} and PV_{mo}—that is, the areas within the TC where these components are actually produced or destroyed. In the following four subsections we evaluate the tendencies of PV_{diab} and PV_{mo}, relate them to physical processes, and infer the contributions of specific PV_{diab} and PV_{mo} features to the cyclone intensity.

3.3.1 Inner-core bulb of negative PV_{diab}

One of the most striking features in PV_{diab} (middle column of Fig. 3) is the eye region, which is dominated by a progressively expanding bulb of negative values. Liu et al., (1997) analysed Hurricane Andrew (1992) and discussed the eye's thermal structure, where a temperature inversion separates a shallow pool of warm, moist air below from a deep layer of warm, dry air aloft. To better understand the origin of PV_{diab}, Fig. 5 shows the six-hour averages of G_{diab} (as defined in Eq. 4) and the corresponding diabatic temperature tendencies T_{diab} for the

https://doi.org/10.5194/egusphere-2026-4860
Preprint. Discussion started: 20 August 2026
© Author(s) 2026. CC BY 4.0 License.

periods preceding the reference times t_0–43 h, t_0, and t_0+31 h. From PV perspective, the origin of PV destruction tendencies (negative G_{diab}) is located primarily near the ocean surface (see bottom row), within a radius of about 25 km at t_0–43 h, extending to 50 km at t_0, and t_0+31 h from the cyclone centre, across all three panels. To further investigate the processes responsible for this positive production, Fig. 6 decomposes G_{diab} at t_0 into its three additive components: G_{mp}, G_{lw}, and G_{bl} (with G_{sw} omitted due to its negligible contribution). Figure 6 further suggests that these negative values result from negative G_{mp} and G_{lw}, partially offset by positive G_{bl}. All three contributions occur within the lowest few metres of the atmospheric surface layer, where T_{mp}, T_{lw}, and T_{bl} exhibit steep vertical gradients. In fact, positive G_{bl} corresponds to rapidly increasing turbulent heat fluxes immediately above the ocean surface. Conversely, negative G_{lw} arises from sharp decreases in longwave radiative heating due to water vapour absorption (resulting in positive T_{lw} in the first model levels), while negative G_{mp} reflects vertically decreasing evaporative cooling. Indicatively, the extremely high values at the first model level (10m asl) reach a maximum of about 740 PVU h^{-1} for G_{bl}, and minima of -160 PVU h^{-1} for G_{mp} and -1000 PVU h^{-1} for G_{lw}.

At t_0–43 h, this inner-core bulb already incorporates negative PV_{diab}, clearly related to negative G_{diab} near the ocean surface (lower-left panel of Fig. 5). At maturity, the negative PV_{diab} bulb has expanded substantially (magenta contour in the middle panel of Fig. 5 extending to ~30 km from the centre), encompassing now a broader portion of the convective eyewall, including areas of positive G_{diab} at the cloud base. Given the clear bottom-up development of the inner-core bulb of negative-PV_{diab} in Figs 2 and 3, it is plausible that air–sea interactions play a leading role in its formation. In this interpretation, negative G_{diab} generated at the ocean surface is advected inward and accumulated near the cyclone centre, facilitated by the dominant radially inward near-surface flow driven by Ekman pumping (not shown). It is noteworthy that above the inner-core bulb of negative PV_{diab}, positive values are found within a layer of about 3 km extending between 2.7 and 5.7 km of altitude (Fig. 4). In fact, there is little to no PV_{diab} production within this elevated region of the TC eye (i.e., a lack of positive G_{diab} in Fig. 5), such that the positive PV_{diab} generated within the lowest atmospheric layers of the eyewall is advected upward and inward over the negative-PV bulb. This upward and inward transport helps produce the characteristic “bowl-shaped” pattern of high PV values shown in Fig. 3d. The subsequent evolution of PV_{diab} within the eye is likely governed by the interplay between inward transport from the eyewall and the eye's

https://doi.org/10.5194/egusphere-2026-4860
Preprint. Discussion started: 20 August 2026
© Author(s) 2026. CC BY 4.0 License.

secondary circulation, which plausibly redistributes positive PV_{diab} downward through subsidence while transporting negative PV_{diab} upward from the lowest atmospheric layers.

3.3.2 The convective eyewall of positive PV_{diab}

At all three times shown in Fig. 5, the predominantly positive T_{diab} values clearly outline the convective eyewall (black contours), coincident with the area of strong ascent (blue contours in Fig. 3). Because the region is dominated by cyclonic flow, Eq. 4 implies that the sign of G_{diab} depends largely on the orientation of the vertical and radial gradients of T_{diab}. In this context, we identify the lowest ~1 km above the surface as the primary area where PV_{diab} is produced (i.e., positive G_{diab} in the lower panels of Fig. 5) with a secondary production area centred at around ~3 km altitude. In both these areas, the strongest positive values of G_{diab} occur at the system's mature stage (t_0; panels in the middle column of Fig. 5).

Figure 6 shows that microphysical processes and boundary-layer turbulent heat fluxes are the dominant contributors to PV_{diab} production within the lowest km and within the eyewall (bottom panels of Fig. 6). Specifically, G_{mp} shows its largest positive values between ~50 and 500 m altitude, reaching a local maximum of 2400 PVU h^{-1}. These positive values arise from a positive vertical gradient in latent heating (T_{mp}), produced first by negative T_{mp} tendencies that are maximum at the surface (0–100 m, dashed black contours associated with rain evaporation), followed by increasing positive T_{mp} (solid contours associated with latent heat release during low-level cloud formation). Between ~500 and 800 m of altitude, G_{bl} becomes positive, reflecting a positive vertical gradient of turbulent heat fluxes (T_{bl}) which shows decreasing negative values with height. It is important to note, however, that the positive PV production from G_{mp} is partially offset by negative G_{bl} values (blue shading) occurring within the lowest 500m of the eyewall area, reaching a local minimum of -1600 PVU h^{-1}. As a result, latent heating (T_{mp}) and turbulent heat fluxes (T_{bl}) are of central importance for both the production and destruction of PV_{diab}, and eventually for shaping the overall PV budget of the TC system, as shown in Fig. 4.

Figure 5 shows a secondary PV source, located near ~3 km altitude at t_0-43h, ~2-3km at t_0 and at ~3km at t_0+31h . Figure 6 (top left panel) directly relates this source to latent heat release, associated with positive vertical gradients of T_{mp}, extending upward to approximately 5 km, where the melting layer is collocated with an area of increasing condensation (not shown). PV_{mp} production at a similar altitude has been also observed by Dearden et

https://doi.org/10.5194/egusphere-2026-4860
Preprint. Discussion started: 20 August 2026
© Author(s) 2026. CC BY 4.0 License.

al. (2016) in the PV towers of two summertime extratropical cyclones, mainly due to cloud condensation and ice deposition (their figure 20). Negative G_{diab} values at t_0 (Fig. 5, top middle panel) occur systematically above ~5 km, with the most pronounced negative values found near the upper layers of the eyewall (12–15 km). Figure 6 relates these negative G_{diab} values to negative vertical gradients of latent heating at the top of convection (top left panel), and to cloud-top radiative cooling between 15 and 18 km (top middle panel). Although Fig. 5 suggests that PV destruction (negative G_{diab}) occurs between ~5 and 12 km, this layer nevertheless contains positive PV_{diab} values (middle panels of Fig. 3). It is therefore plausible that a substantial portion of PV_{diab} produced within the lowest km of the convective eyewall is continually advected upward, where it is progressively destroyed near the top of convection. Because the upward flux of PV_{diab} exceeds its destruction by G_{diab}, the eyewall is dominated by positive PV values and thus contributes positively to the TC's cyclonic circulation.

3.3.3 The special role of PV_{mo} in TC development

The role of diabatic processes in forming distinct dynamical substructures of opposite signs is evident and discussed above. In contrast, PV_{mo} is mainly contributing with positive values in areas that extend over the inner core bulb of negative PV_{diab}. Indeed, Fig. 3f shows positive PV_{mo} values that completely cover the negative PV_{diab} values in Fig. 3e and slightly extend upwards, further contributing to the "bowl" shape of high PV values in Fig. 3d. To better understand the areas responsible for the production of PV_{mo}, Fig. 7 shows G_{mo} tendencies at three different times while the following equation expands the second right-hand side of Eq. 7 in radial coordinates (assuming asymmetry):

$$G_{mo} = \frac{1}{\rho}\frac{1}{r}\left(\frac{\partial \boldsymbol{F}_{\varphi}}{\partial r}\frac{\partial \theta}{\partial z} - \frac{\partial \boldsymbol{F}_{\varphi}}{\partial z}\frac{\partial \theta}{\partial r}\right), \qquad \text{Eq. 7}$$

where r is the radius from the TC centre. Figure 7 clearly shows that most of the positive G_{mo} (i.e., PV_{mo} production) occurs within the lowest atmospheric layers, below approximately 500 m. In the early stage (t_0-43 h), PV_{mo} production is concentrated near the surface and is directly advected toward the TC centre. In the two later stages (middle and right panels of Fig. 7), PV_{mo} production remains confined to the first 500 m above the ocean surface. At t_0, PV_{mo} production is evidently associated with frontal regions characterised by strong horizontal gradients of θ (thick grey lines) and sharp vertical gradients of $\boldsymbol{F}$. The second term of Eq. 7 is likely the dominant

https://doi.org/10.5194/egusphere-2026-4860
Preprint. Discussion started: 20 August 2026
© Author(s) 2026. CC BY 4.0 License.

contributor to positive PV_{mo} production, arising from the interaction between the negative horizontal θ gradient—formed between the warm core of the TC and the colder surrounding environment—and the negative vertical gradient of $\boldsymbol{F}$, which relates to frictional forces decreasing with height. The formation of the horizontal θ gradient can be linked to different physical processes. Figure 8 displays the individual θ-tracers that collectively yield the total θ (θ_{sw} is small and thus omitted). Across all three stages, the near-surface warm core can be primarily attributed to θ_{bl}, i.e., sensible heat fluxes and turbulent diffusion of temperature. In contrast, microphysical processes (θ_{mp}) tend to cool the lower levels, contributing to a cold-core structure near the surface, while above ~2 km they contribute positively to the warm core. Consequently, sensible heat fluxes and turbulent temperature diffusion emerges as the main drivers shaping the near-surface warm core and thus the frontal zone where PV_{mo} production is enhanced. Notably, at t_0, PV_{mo} production occurs within the inner core of the negative-bulb PV_{diab} (outlined by the magenta contour in Figs 5 and 7), whereas by t_0+31 h, production is largely excluded from the inner core. Simultaneously, positive PV_{diab} production is also absent from the inner core—except for the negative PV_{diab} production very close to the surface (blue shading in Fig. 5). Altogether, these results support the interpretation that cyclone decay begins once positive PV sources are excluded from the inner core.

3.3.4 The contributions of PV_{diab} and PV_{mo} to cyclone intensity

To further investigate the contribution of the inner-core bulb of negative PV_{diab} to the cyclone's maximum intensity, Figs 9a and 9b show the tangential wind field inferred from the ensemble of U-Net models performing piecewise PV inversion (described in Section 2.3 and Section S4 of the Supplementary Material). Both panels are based on the PV structure constructed in axisymmetric coordinates from the radially averaged θ and tangential wind fields of the WRF simulation of Usagi at t_0. However, the definition of the inner bulb (outlined by the green dashed contour) differs for the two panels, defined in Fig. 9a as the region overlapping with the negative PV_{diab} shown in Fig. 3e. Although Fig. 3f indicates a close correspondence between the negative PV_{diab} and the highest positive values of PV_{mo}, the latter extends to slightly higher altitudes, bounded by a pronounced PV_{mo} gradient. Alternatively, if the edge of the inner-core bulb is arbitrarily defined by the PV_{mo} equalling 2.5 PVUs, the bulb extends to higher altitudes (compare the dashed contours in Figs 9a and 9b), thereby encompassing a region of relatively large PV where high PV_{mo} values are superimposed with positive PV_{diab}. In both definitions, the

https://doi.org/10.5194/egusphere-2026-4860
Preprint. Discussion started: 20 August 2026
© Author(s) 2026. CC BY 4.0 License.

contribution of the inner-core bulb to the cyclone's maximum wind speed (approximately 65 m s^{-1}) remains relatively modest, accounting for about 10% in Fig. 7a and 15% in Fig. 7b.

Regarding the contribution of PV_{mo} to TC intensity, we further employ the U-Net piecewise PV inversion by defining a PV anomaly that excludes the inner-core bulb of negative PV_{diab}. Outside this region, the amplitude of the total PV is reduced to match the ratio of PV_{mo} to total PV diagnosed from the WRF simulation (i.e., the ratio between the fields shown in Figs. 3f and 3e, excluding the inner-core bulb defined in Fig. 9a). The resulting PV anomaly is shown in Fig. 9c. It is substantially weaker than the total PV fields shown in Figs. 9a and 9b, while retaining the high PV_{mo} values located between the dashed contours in those panels. The tangential wind field inferred from this PV anomaly extends throughout the atmospheric column, with a local maximum naturally concentrated near the region of maximum PV_{mo}. The inferred wind field indicates that PV_{mo}, excluding the inner-core bulb of negative PV_{diab}, contributes approximately 15% to the cyclone's maximum intensity. The remainder of the TC PV field, including PV_{diab} and the inner-core bulb (a positive PV substructure outlined by the dashed contour in Fig. 9a), is responsible for the remaining ~85% of the cyclone intensity and closely reproduces the entire cyclonic circulation (Fig. 9d). Our results in Fig. 9 tend to agree with the analytical piecewise PV inversion used by Shi and Chen (2021), based on Kieu and Zhang, 2010), who found diabatic heating driving TC intensification whereas an inner core PV anomaly contributes mostly to forming maximum wind speed at lower atmospheric levels.

Although the U-Net exhibits only a small residual error when performing piecewise PV inversion for the cases of the inner-core bulb of negative PV_{diab} and the fraction of PV_{mo} (Fig. S3 in the supplementary material), it was trained on CM1 simulations to reconstruct the cyclone tangential wind field, whereas the boundaries of the inner-core bulb are defined from the WRF simulation. Due to these inconsistencies, these percentages should be interpreted as order-of-magnitude estimates rather than precise quantifications of the contribution of the two PV anomalies to the maximum intensity of tropical cyclones. Even at this level of precision, however, they place momentum forcing in perspective: although latent heat release remains the dominant PV source, of the order of a quarter of the cyclone's peak intensity originates from processes confined to the lowest few hundred metres above the ocean. That contribution is itself a residual of two opposing tendencies, G_{mo} and G_{lw}, each exceeding several hundred PVU h^{-1} near the surface. TC intensity is therefore set not only by eyewall convection but by a finely

https://doi.org/10.5194/egusphere-2026-4860
Preprint. Discussion started: 20 August 2026
© Author(s) 2026. CC BY 4.0 License.

balanced near-surface competition, which locates a first-order source of intensity uncertainty in the eye rather than the eyewall.

4. Conclusions

Cyclone dynamics can be regarded as an ensemble of interacting PV anomalies. In this framework, the PV anomalies governing TC development arise primarily from diabatic heating (i.e. PV_{diab}) and momentum forcing (PV_{mo}) associated with exchanges of heat and momentum between the atmosphere and the underlying ocean. In both TCs analysed, these processes consistently build the cyclone as a coherent positive PV anomaly throughout the troposphere, providing a process-based framework for characterising the evolution of TC structure and intensity.

Generalising beyond the two case studies considered here, our results suggest that TC intensification begins with the formation of a vertically coherent PV tower generated by latent heat release within deep convection. As intensification proceeds, the cyclone progressively acquires an increasingly axisymmetric structure, with its maximum winds becoming organised around the convective eyewall. At maturity, the PV anomaly evolves into a characteristic "bowl-shaped" structure composed of three dynamically distinct regions: (i) a lower inner-core bulb characterised by comparatively weak positive PV within the lowest 2–3 km of the eye, (ii) the remainder of the eye above this bulb, and (iii) the surrounding convective eyewall, where large positive diabatically generated PV dominates and extends vertically through much of the troposphere.

Although this study does not address the mechanisms responsible for TC genesis or axisymmetrisation, our results indicate that the establishment of an approximately symmetric vortex is essential for the development of the near-surface Ekman inflow. This circulation continuously transports heat and PV towards the cyclone centre and thereby maintains the mature PV structure. Sensible heat fluxes contribute to the development of the low-level warm core, imposing thus a baroclinic area with the colder environment. This baroclinic area interacts with frictional deceleration to generate positive PV_{mo} near the ocean surface beneath the eyewall. Positive PV_{mo} is subsequently advected inward and contributes constructively to cyclone development. At the same time, strong near-surface temperature gradients produced primarily by longwave radiative cooling generate negative PV_{diab} beneath the eyewall. These anomalies are likewise advected towards the cyclone centre, where they partially

https://doi.org/10.5194/egusphere-2026-4860
Preprint. Discussion started: 20 August 2026
© Author(s) 2026. CC BY 4.0 License.

offset the positive, frictionally generated PV_{mo}. The balance between these competing contributions produces the characteristic low-PV inner-core bulb within the eye. Simultaneously, deep convection within the eyewall continuously generates large positive PV_{diab} through latent heat release and turbulent heat fluxes. Together with the frictionally generated PV_{mo} produced near the ocean surface, these anomalies are transported upward along the eyewall and inward through the middle troposphere over the inner-bulb, maintaining the bowl-shaped PV structure that characterises mature TCs. Our results therefore identify both air–sea interactions and eyewall convection as persistent and important sources and sinks of the PV budget that together sustain TCs throughout their life cycle. A machine learning model, based on a U-Net that we trained using idealised simulations, suggests that the PV within the inner-bulb together with the PV_{mo} within the eye contribute together by an order of 20% to the cyclone maximum intensity.

From the perspective of PV invertibility, the cyclone reaches maximum intensity in Fig. 2 when average vertical PV structure attains maximum amplitude. This amplitude reflects the combined effects of two competing mechanisms: the balance between frictionally generated positive PV and diabatically generated negative PV within the inner core, and the continued production of large positive diabatic PV by deep convection within the eyewall. Air–sea interactions primarily regulate the former through their control of the warm core and associated baroclinicity, whereas latent heating controls the latter. Our results further suggest that the accumulation of negative diabatic PV within the inner core gradually weakens the bowl-shaped PV structure. Once this coherent structure can no longer be maintained, cyclone intensity decreases and the system enters its decay phase.

Overall, our findings indicate that TC intensity is consistent with the evolution of a coherent scheme of interacting PV substructures that are generated by several physical processes. While convection provides the dominant source of positive PV throughout the cyclone life cycle, air–sea interactions modulate how this PV is shaped and maintained within the inner core. Future studies will aim to address several questions that remain open, including the mechanisms allowing frictionally generated PV to exceed the magnitude of the opposing diabatic contribution near the surface, the individual dynamical roles of the identified PV substructures, and the processes governing the eventual collapse of the bowl-shaped PV structure that marks the onset of cyclolysis.

https://doi.org/10.5194/egusphere-2026-4860
Preprint. Discussion started: 20 August 2026
© Author(s) 2026. CC BY 4.0 License.

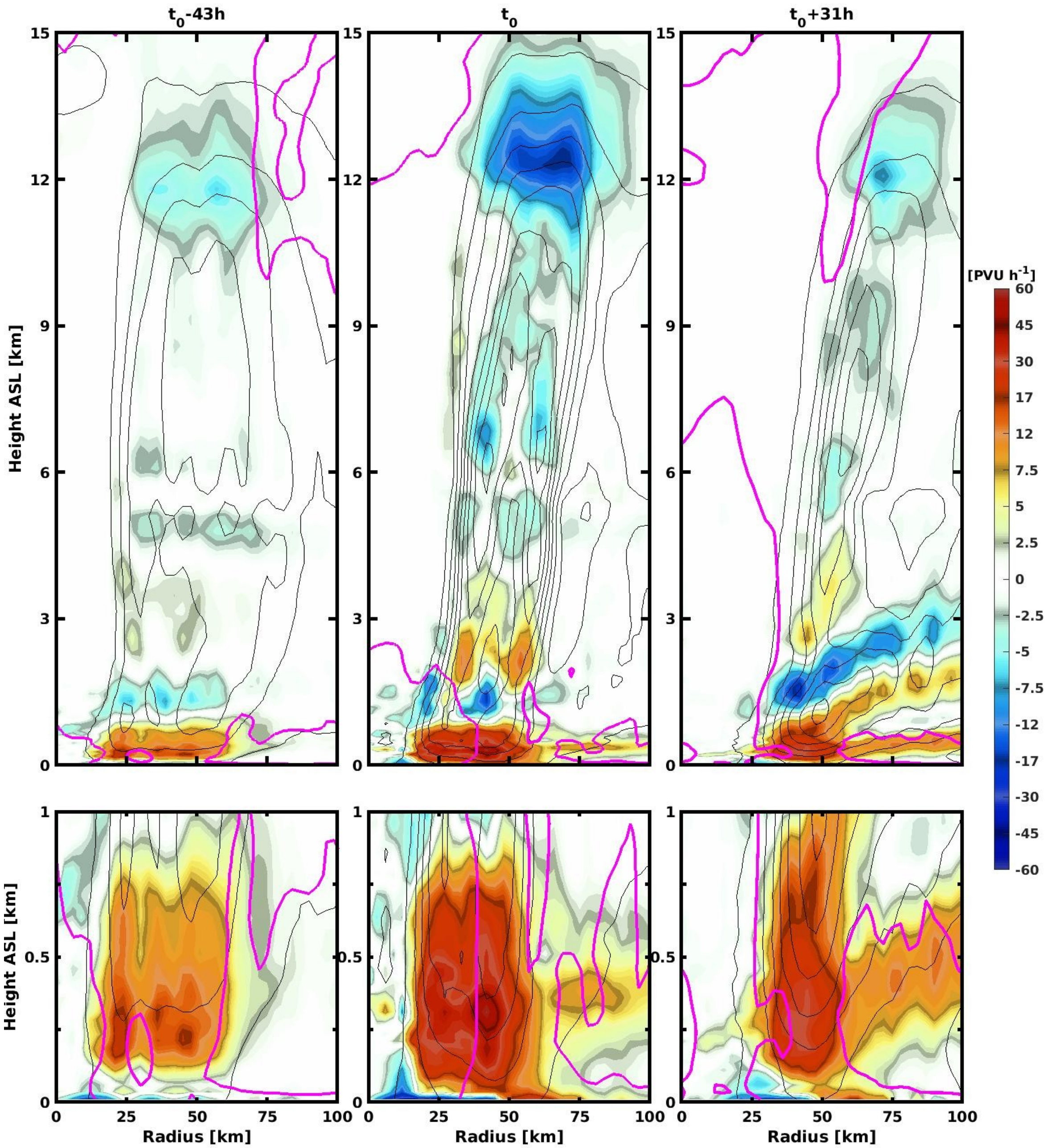

Figure 5: Vertical-radial distribution of the azimuthal mean of diabatically produced PV tendencies (G_{diab} in eq. 3, shown in colour) for TC Usagi at the three selected times. Solid black contours represent T_{diab} with an interval of 3 K h^{-1}, starting from 1 K h^{-1}. All fields are averaged over the six hours preceding the times indicated in the title, where t_0 marks the mature stage. To delineate the inner-core (see text), the magenta contour represents the zero isoline of 6-hourly average PV_{diab} prior to the times shown in the top panel titles. The bottom panels provide a zoomed-in view of the first km asl shown in the top panels.

https://doi.org/10.5194/egusphere-2026-4860
Preprint. Discussion started: 20 August 2026
© Author(s) 2026. CC BY 4.0 License.

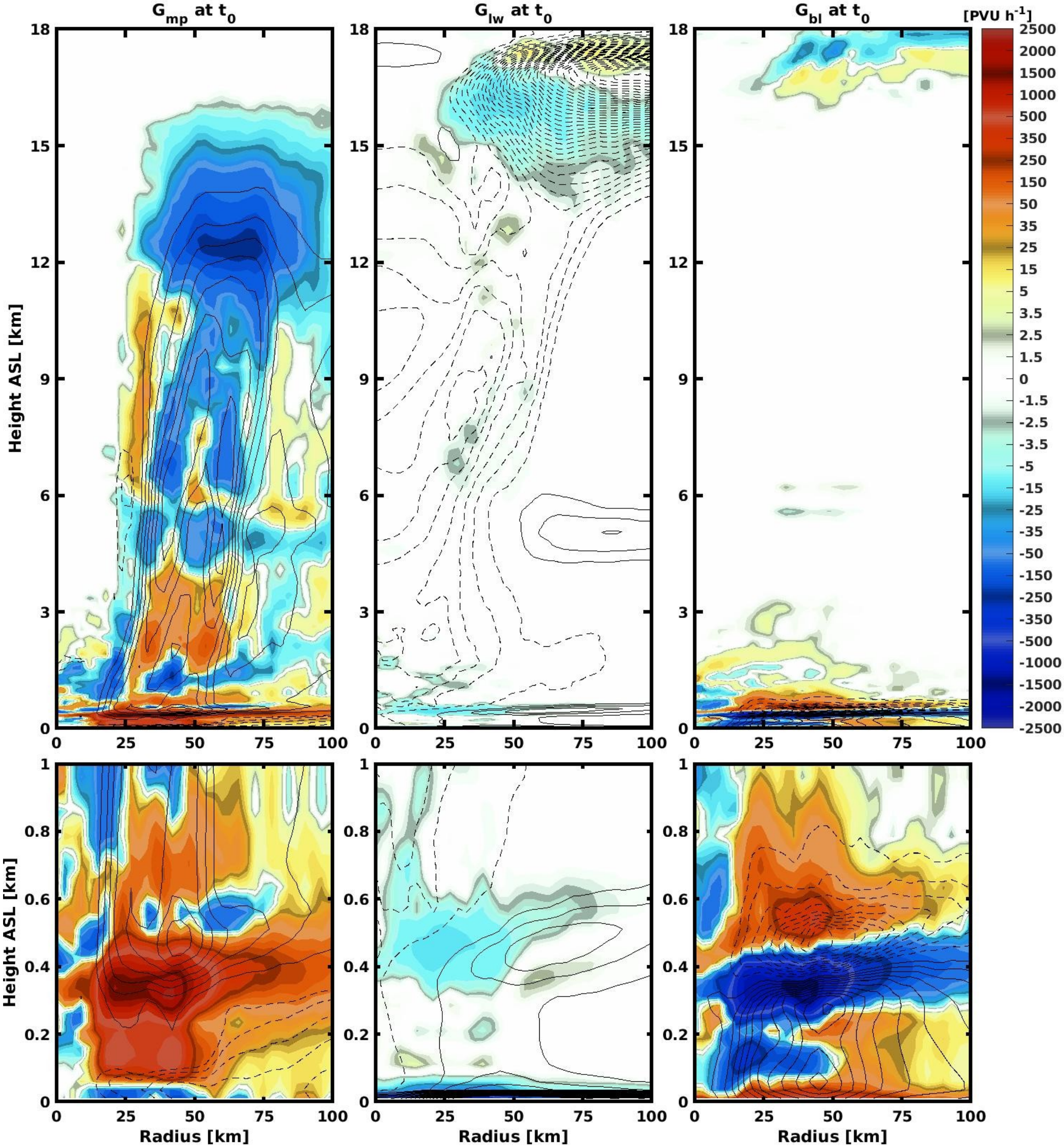

Figure 6: As for Fig. 5 but for the azimuthal mean G_{mp} (left panels), G_{lw} (middle panels) and G_{bl} (right panels) in colour shading with the corresponding values of temperature tendencies (T_{mp}, T_{lw}, T_{bl}) in black contours. Contour intervals are different in each panel. Left panel: every 40 K h^{-1} (-5 K h^{-1}) for positive (negative) values; Middle panel: every 0.5 K h^{-1} (-0.5 K h^{-1}) for positive (negative) values; Right panel: every 10 K h^{-1} (-10 K h^{-1}) for positive (negative) values; all averaged over the six hours preceding t_0.

https://doi.org/10.5194/egusphere-2026-4860
Preprint. Discussion started: 20 August 2026
© Author(s) 2026. CC BY 4.0 License.

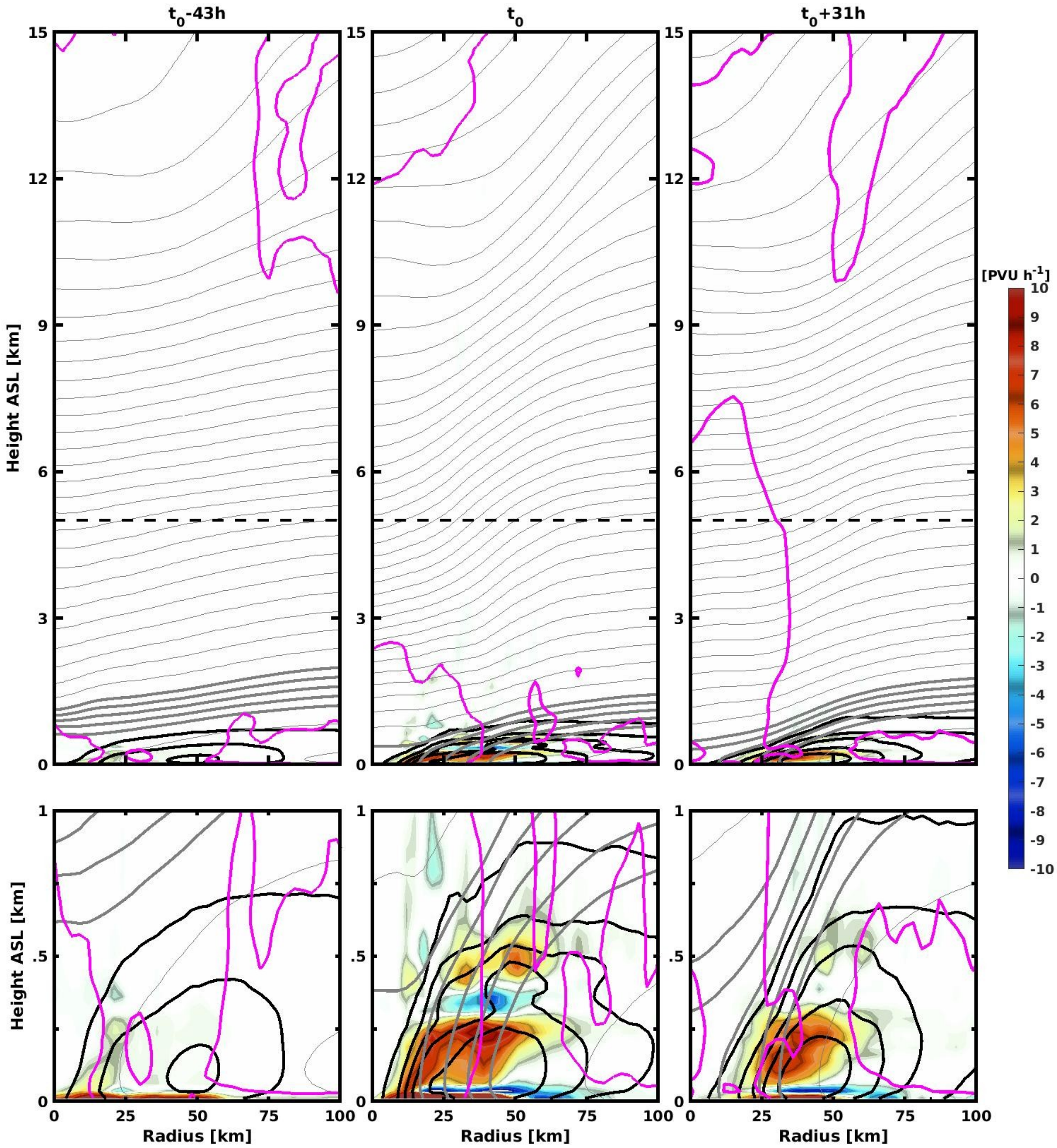

655 **Figure 7: Vertical-radial distribution of the azimuthal mean of momentum produced PV tendencies (G_{mo} in eq. 3, shown in colour) for TC Usagi at the three selected times. Black contours represent azimuthal mean tangential F with intervals of -10, -7, -5, -3 and -1 m s^{-2} and grey contours represent θ with an interval of 1 K, starting (thicker contours are used for values between 306-310 K). All fields are averaged over the six hours preceding the times indicated in the title, where t_0 marks the mature stage. To delineate the inner-core (see text), the magenta contour represents the zero isoline of 6-hourly average PV_{diab} prior to the times shown in the top panel titles. The bottom panels provide a zoomed-in view of the first km asl shown in the top panels.**

https://doi.org/10.5194/egusphere-2026-4860
Preprint. Discussion started: 20 August 2026
© Author(s) 2026. CC BY 4.0 License.

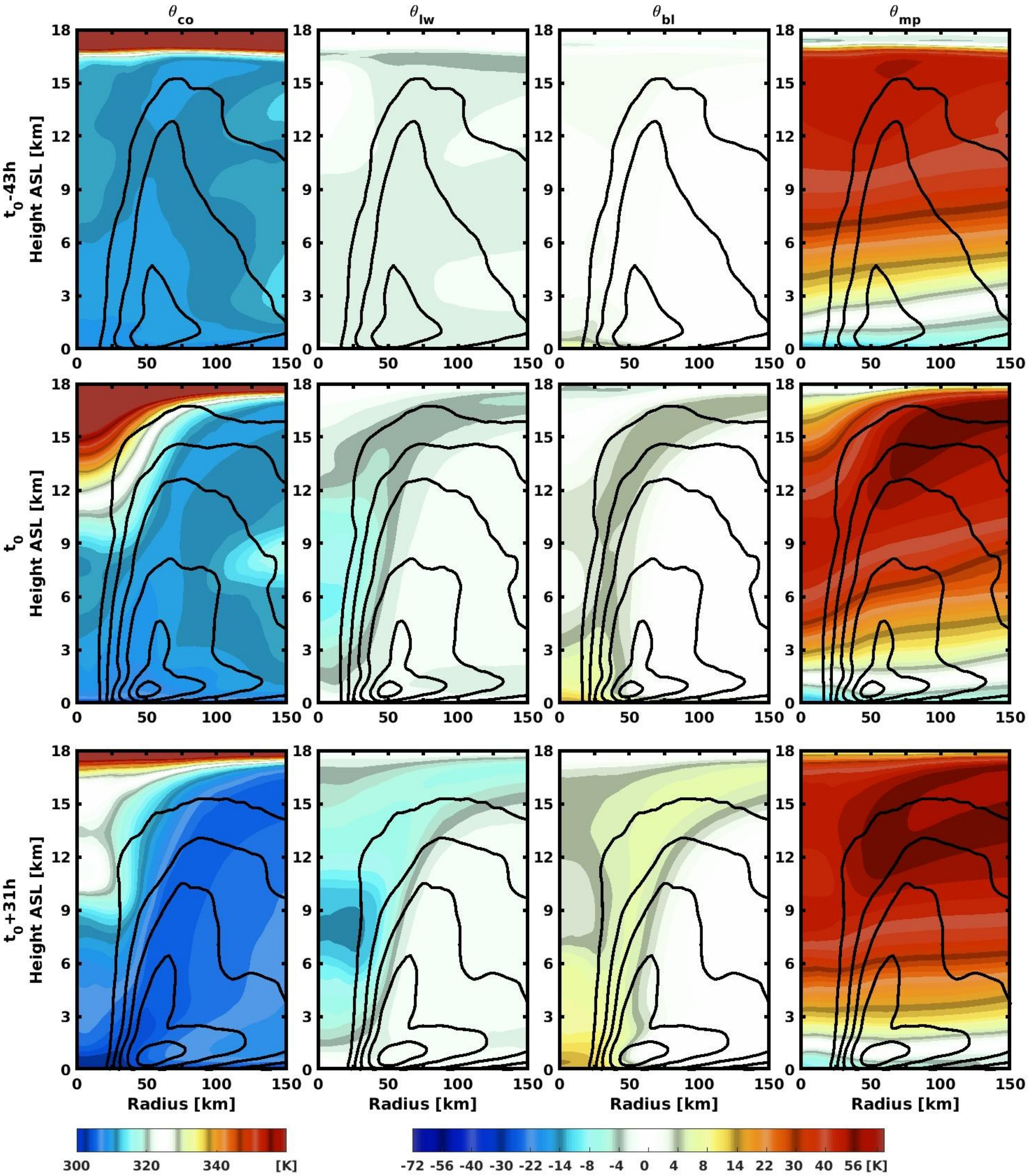

Figure 8: Vertical-radial distribution of the azimuthal mean θ tracers (columns) for TC Usagi and for three different times (rows). Black contours show azimuthal mean tangential wind speed (every 10 m s^{-1}, starting from 20 m s^{-1}). Fields of θ_{sw} are comparably small and thus are not shown.

https://doi.org/10.5194/egusphere-2026-4860
Preprint. Discussion started: 20 August 2026
© Author(s) 2026. CC BY 4.0 License.

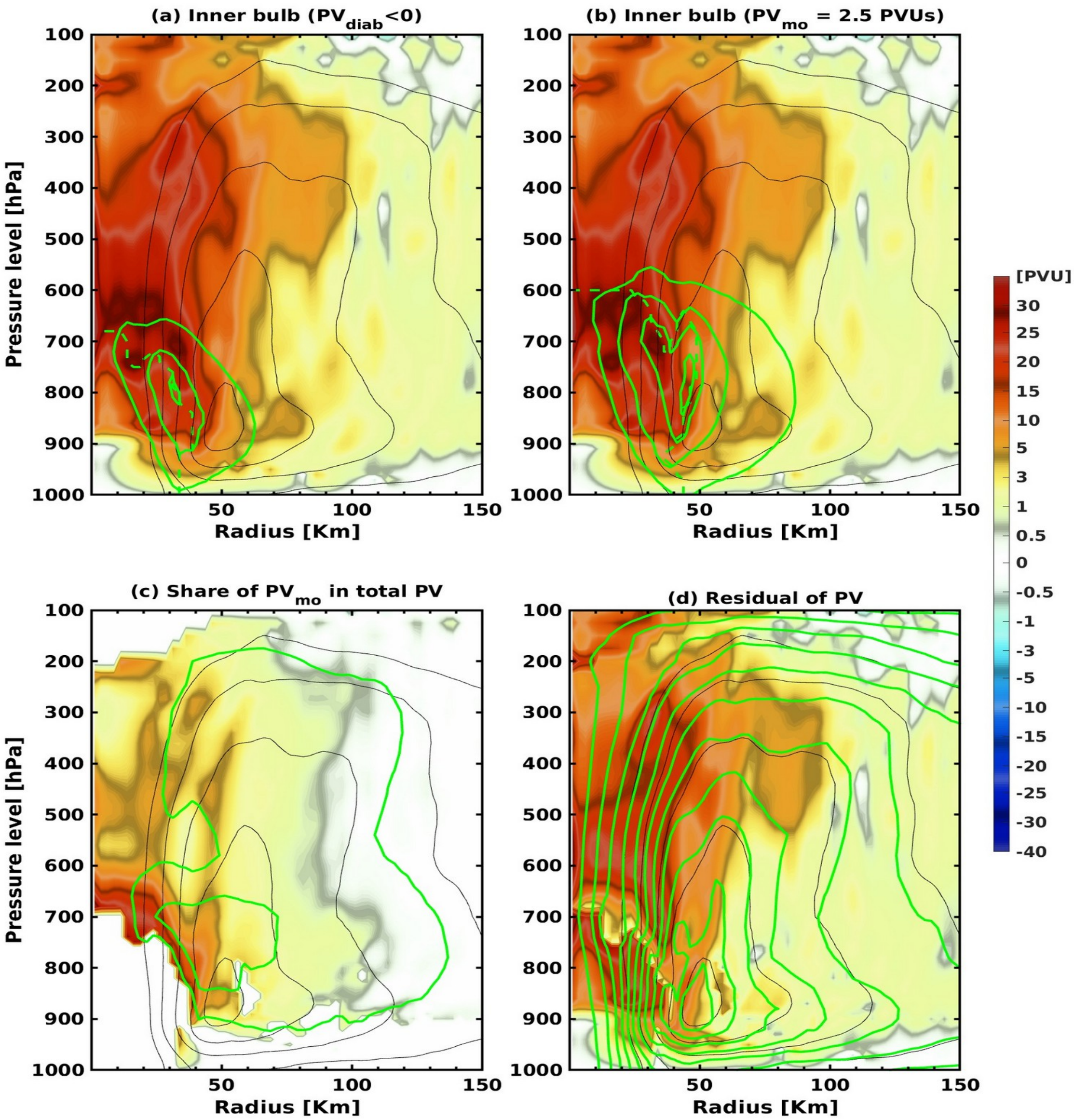

Figure 9: Attribution of the intensity (tangential wind field) of TC Usagi at t_0 to various PV fields computed using the radially averaged WRF θ and tangential wind speed. Each panel shows two tangential wind fields: the wind field attributed to the full PV field (black contours with a 10 m s^{-1} interval, starting at 25 m s^{-1}, identical for all panels) and the wind field attributed to a portion of the full PV field (green contours with 5 m s^{-1} interval, starting at 5 m s^{-1}). The portions of the PV fields are a the inner bulb region enclosed by the green dashed contour of the full PV field (shown in colour), b as for a but for a different definition of the inner bulb, c share of the full PV field in a, b due to momentum forcing excluding the inner bulb region in b (shown in colour), and d remainder of the full PV field in a, b when the PV field in c is removed (shown in colour). In all panels the tangential wind speeds are inferred by an ensemble of U-Net models from the given PV field.

https://doi.org/10.5194/egusphere-2026-4860
Preprint. Discussion started: 20 August 2026
© Author(s) 2026. CC BY 4.0 License.

Appendix A

PV budget and its residual: At the end of each model time step, PV is calculated directly from the model output fields as in Eq. 1. This PV is shown in the left column of Figs. A1 and A2. Ideally, the sum of all PV tracers (middle columns of Figs. A1 and A2) should reproduce this total PV field. However, differences remain, and therefore the PV budget has a residual term (right columns of Figs. A1 and A2), as described in Section 2. For Usagi (Fig. A1), q_r remains relatively small during the intensification stage and increases during maturity, mainly within the cyclone centre at a radius of approximately 25–50 km and at an altitude of around 3 km. This corresponds to the region of higher PV (left panel at t_0) and also extends along the convective eyewall. During the decay stage, the residual becomes larger in the region extending beyond the convective eyewall, while the inner core remains associated with comparatively small residual. For Katrina (Fig. A2), the intensification phase is also characterised by relatively small residual values (Fig. A2, top right panel). However, the mature stage shows relatively large positive residual within the cyclone inner core, together with negative values along the convective eyewall. A similar pattern, although with smaller amplitude, is also present during the decay stage, suggesting that residual is increasing mainly during cyclone intensification. In both cases, the residual can locally reach significant values. Nevertheless, the sum of PV-tracers shown in the middle panels of Figs. A1 and A2 reproduces a spatially consistent structure to total PV (left column of panels) for both cyclones, clearly identifying the areas of high and low PV.

https://doi.org/10.5194/egusphere-2026-4860
Preprint. Discussion started: 20 August 2026
© Author(s) 2026. CC BY 4.0 License.

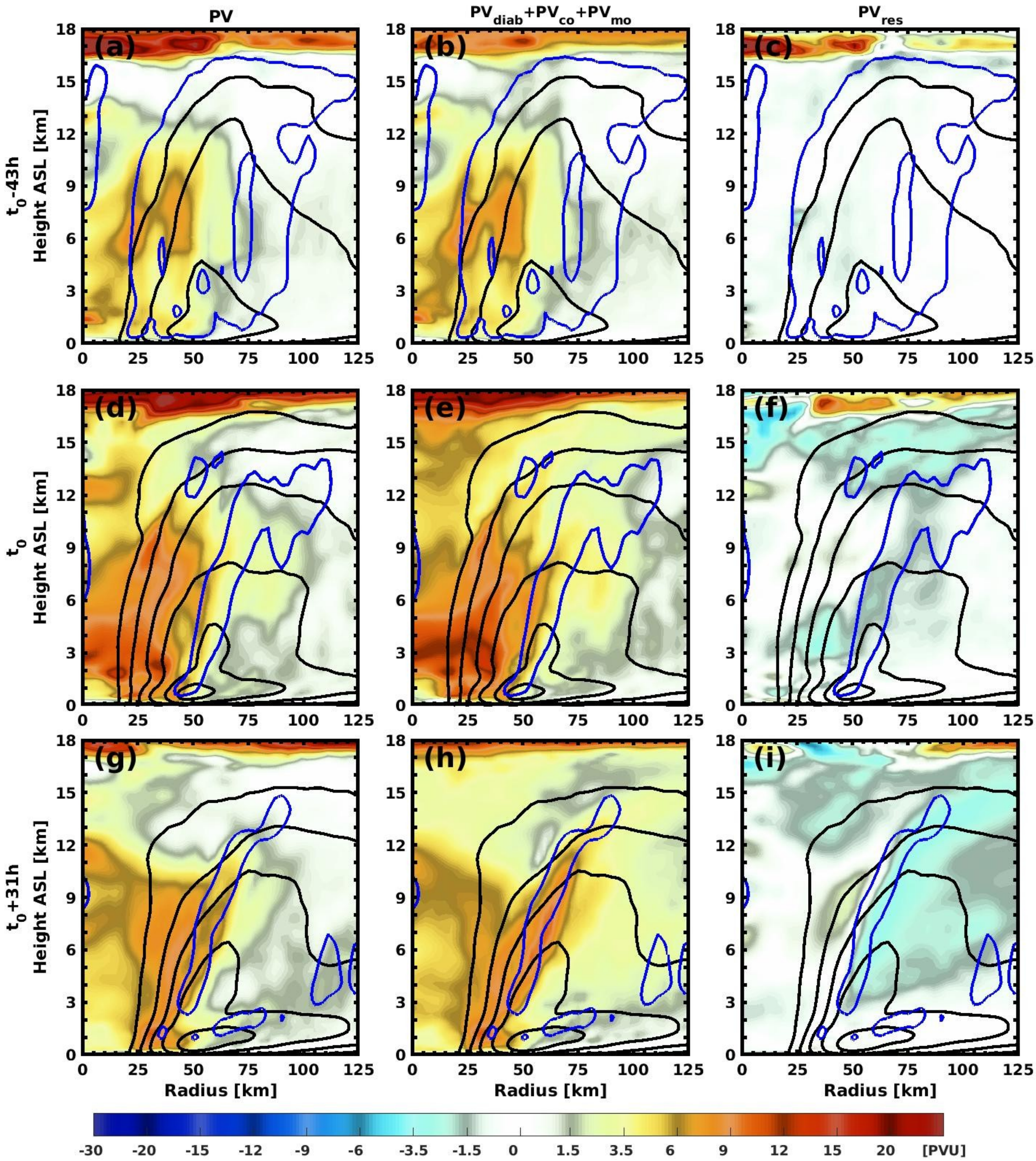

Figure A1: Vertical-radial distribution of winds, total PV, and residual in TC Usagi. Colour shading is total PV, the sum of PV_{co}, PV_{diab} and PV_{mo}, and PV_{res}, in the left, middle and right columns, respectively. Each row of panels refers to different times with respect to the mature stage (t_0; see text). Panels also show azimuthal mean tangential wind speed (in black contours every 10 m s^{-1}, starting from 20 m s^{-1}) and vertical wind speed for 0.25 m s^{-1} and 0.75 m s^{-1} (in blue contours).

https://doi.org/10.5194/egusphere-2026-4860
Preprint. Discussion started: 20 August 2026
© Author(s) 2026. CC BY 4.0 License.

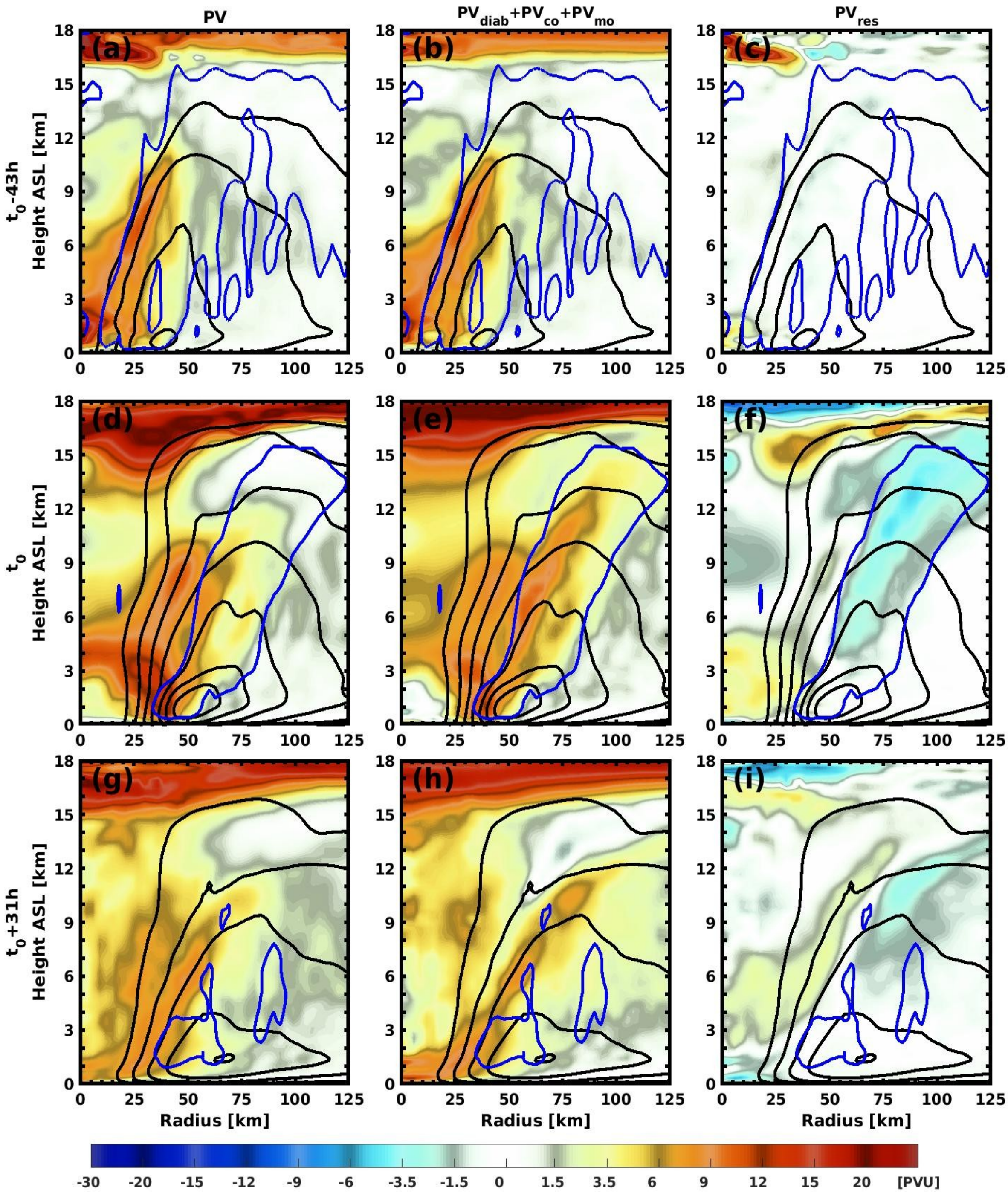

Figure A2: As in Fig. A1 but for TC Katrina.

https://doi.org/10.5194/egusphere-2026-4860
Preprint. Discussion started: 20 August 2026
© Author(s) 2026. CC BY 4.0 License.

Code and data availability

The original WRF code is available under UCAR Open Source License (https://github.com/wrf-model/WRF/releases#release-v4.4.2). In the supplement we provide a .zip file with all WRF modules for version 4.4.2 that allow reproduction of our simulations, including PV and θ tracer diagnostics. We also provide the two namelists that we used to perform the simulations. A Readme file provides all necessary instructions.

Supplement link

The link to the supplement will be included by Copernicus, if applicable.

Author contributions

EF conceived this study, developed the PV-tracers code for WRF and performed the simulations. EF wrote first draft of the paper with substantial contributions from SLG on the interpretation of PV-tracers and TC dynamical substructures.

Competing interests

The authors declare that they have no conflict of interest.

Acknowledgements

This paper has been a long-standing effort enriched by sporadic discussions in the last four years during MedCyclones COST Action. EF is grateful to Stavros Dafis for early discussions on the physical interpretation of PV tracers and to Kerry Emanuel for exchanges during the TROPICANA project (TROPIcal Cyclones in ANthropocene: physics, simulations & Attribution).

https://doi.org/10.5194/egusphere-2026-4860
Preprint. Discussion started: 20 August 2026
© Author(s) 2026. CC BY 4.0 License.

Financial support

EF was supported by the ESA Medicanes project ESA Contract No. 4000144111/23/I-KE. SLG was supported by the UKRI Natural Environment Research Council (NERC), grant number: NE/Z000092/1.

References

Adamson, D. S., Belcher, S. E., Hoskins, B. J., and Plant, R. S.: Boundary-layer friction in midlatitude cyclones, Q. J. Roy. Meteorol. Soc., 132, 101–124, https://doi.org/10.1256/qj.04.145, 2006.

Agusti-Panareda, A., Thorncroft, C. D., Craig, G. C., and Gray, S. L.: The extratropical transition of hurricane Irene (1999): A potential-vorticity perspective, Quart J Royal Meteoro Soc, 130, 1047–1074, https://doi.org/10.1256/qj.02.140, 2004.

Agustí-Panareda, A., Gray, S. L., Craig, G. C., and Thorncroft, C.: The Extratropical Transition of Tropical Cyclone Lili (1996) and Its Crucial Contribution to a Moderate Extratropical Development, Monthly Weather Review, 133, 1562–1573, https://doi.org/10.1175/MWR2935.1, 2005.

Bracegirdle, T. J. and Gray, S. L.: The dynamics of a polar low assessed using potential vorticity inversion, Quart J Royal Meteoro Soc, 135, 880–893, https://doi.org/10.1002/qj.411, 2009.

Bhatia, K., Vecchi, G., Murakami, H., Underwood, S., and Kossin, J.: Projected Response of Tropical Cyclone Intensity and Intensification in a Global Climate Model, J. Climate, 31, 8281–8303, https://doi.org/10.1175/JCLI-D-17-0898.1, 2018.

Bryan, G. H.: Effects of Surface Exchange Coefficients and Turbulence Length Scales on the Intensity and Structure of Numerically Simulated Hurricanes, Mon. Wea. Rev., 140, 1125–1143, https://doi.org/10.1175/MWR-D-11-00231.1, 2012.

Bryan G. H.: The Governing Equations for CM1 Version 10 National Center for Atmospheric Research, 2021. https://www2.mmm.ucar.edu/people/bryan/cm1/cm1_equations.pdf (accessed 23 June 2026).

Čampa, J. and Wernli, H.: A PV Perspective on the Vertical Structure of Mature Midlatitude Cyclones in the Northern Hemisphere, J. Atmos. Sci., 69, 725–740, https://doi.org/10.1175/JAS-D-11-050.1, 2012.

Chagnon, J. M., Gray, S. L., and Methven, J.: Diabatic processes modifying potential vorticity in a North Atlantic cyclone, Quart J Royal Meteoro Soc, 139, 1270–1282, https://doi.org/10.1002/qj.2037, 2013.

Chagnon, J. M. and Gray, S. L.: A Diabatically Generated Potential Vorticity Structure near the Extratropical Tropopause in Three Simulated Extratropical Cyclones, Monthly Weather Review, 143, 2337–2347, https://doi.org/10.1175/MWR-D-14-00092.1, 2015.

Chen, S.-H. and Sun, W.-Y.: A One-dimensional Time Dependent Cloud Model, Journal of the Meteorological Society of Japan, 80, 99–118, https://doi.org/10.2151/jmsj.80.99, 2002.

Croad, H. L., Methven, J., Harvey, B., Keeley, S. P. E., and Volonté, A.: The role of boundary layer processes in summer-time Arctic cyclones, Weather Clim. Dynam., 4, 617–638, https://doi.org/10.5194/wcd-4-617-2023, 2023.

Davis, C. A. and Emanuel, K. A.: Potential Vorticity Diagnostics of Cyclogenesis, Mon. Wea. Rev., 119, 1929–1953, https://doi.org/10.1175/1520-0493(1991)119%3C1929:PVDOC%3E2.0.CO;2, 1991.

Davis, C. A.: Piecewise Potential Vorticity Inversion, J. Atmos. Sci., 49, 1397–1411, https://doi.org/10.1175/1520-0469(1992)049%3C1397:PPVI%3E2.0.CO;2, 1992.

Davis, C. A., Stoelinga, M. T., and Kuo, Y.-H.: The Integrated Effect of Condensation in Numerical Simulations of Extratropical Cyclogenesis, Mon. Wea. Rev., 121, 2309–2330, https://doi.org/10.1175/1520-0493(1993)121%3C2309:TIEOCI%3E2.0.CO;2, 1993.

https://doi.org/10.5194/egusphere-2026-4860
Preprint. Discussion started: 20 August 2026
© Author(s) 2026. CC BY 4.0 License.

Dearden, C., Vaughan, G., Tsai, T., and Chen, J.-P.: Exploring the Diabatic Role of Ice Microphysical Processes in Two North Atlantic Summer Cyclones, Monthly Weather Review, 144, 1249–1272, https://doi.org/10.1175/MWR-D-15-0253.1, 2016.

Emanuel, K. A.: An Air-Sea Interaction Theory for Tropical Cyclones. Part I: Steady-State Maintenance, J. Atmos. Sci., 43, 585–605, https://doi.org/10.1175/1520-0469(1986)043%3C0585:AASITF%3E2.0.CO;2, 1986.

Emanuel, K.: Increasing destructiveness of tropical cyclones over the past 30 years, Nature, 436, 686–688, https://doi.org/10.1038/nature03906, 2005.

Flaounas, E., Gray, S. L., and Teubler, F.: A process-based anatomy of Mediterranean cyclones: from baroclinic lows to tropical-like systems, Weather Clim. Dynam., 2, 255–279, https://doi.org/10.5194/wcd-2-255-2021, 2021.

Gopalakrishnan, S.G., Surgi, N., Tuleya, R., Janjic Z.: NCEP's two-way-interactive-moving-nest NMM-WRF modeling system for hurricane forecasting. Preprints, 27th Conf. on Hurricanes and Tropical Meteorology, Monterey, CA, Amer. Meteor. Soc., 7A.3, 2026.

Gray, S. L.: Mechanisms of midlatitude cross-tropopause transport using a potential vorticity budget approach, J. Geophys. Res., 111, 2005JD006259, https://doi.org/10.1029/2005JD006259, 2006.

Hendricks, E. A., Montgomery, M. T., and Davis, C. A.: The Role of "Vortical" Hot Towers in the Formation of Tropical Cyclone Diana (1984), J. Atmos. Sci., 61, 1209–1232, https://doi.org/10.1175/1520-0469(2004)061%3C1209:TROVHT%3E2.0.CO;2, 2004.

Hersbach, H., Bell, B., Berrisford, P., Hirahara, S., Horányi, A., Muñoz-Sabater, J., Nicolas, J., Peubey, C., Radu, R., Schepers, D., Simmons, A., Soci, C., Abdalla, S., Abellan, X., Balsamo, G., Bechtold, P., Biavati, G., Bidlot, J., Bonavita, M., De Chiara, G., Dahlgren, P., Dee, D., Diamantakis, M., Dragani, R., Flemming, J., Forbes, R., Fuentes, M., Geer, A., Haimberger, L., Healy, S., Hogan, R. J., Hólm, E., Janisková, M., Keeley, S., Laloyaux,

https://doi.org/10.5194/egusphere-2026-4860
Preprint. Discussion started: 20 August 2026
© Author(s) 2026. CC BY 4.0 License.

P., Lopez, P., Lupu, C., Radnoti, G., De Rosnay, P., Rozum, I., Vamborg, F., Villaume, S., and Thépaut, J.: The ERA5 global reanalysis, Quart J Royal Meteoro Soc, 146, 1999–2049, https://doi.org/10.1002/qj.3803, 2020.

Hersbach, H., Bell, B., Berrisford, P., Biavati, G., Horányi, A., Muñoz Sabater, J., Nicolas, J., Peubey, C., Radu, R., Rozum, I., Schepers, D., Simmons, A., Soci, C., Dee, D., Thépaut, J-N. (2023): ERA5 hourly data on pressure levels from 1940 to present. Copernicus Climate Change Service (C3S) Climate Data Store (CDS), DOI: 10.24381/cds.bd0915c6 (Accessed on 30-04-2026)

Hong, S.-Y., Noh, Y., and Dudhia, J.: A New Vertical Diffusion Package with an Explicit Treatment of Entrainment Processes, Monthly Weather Review, 134, 2318–2341, https://doi.org/10.1175/MWR3199.1, 2006.

Hoskins, B. J., McIntyre, M. E., and Robertson, A. W.: On the use and significance of isentropic potential vorticity maps, Quart J Royal Meteoro Soc, 111, 877–946, https://doi.org/10.1002/qj.49711147002, 1985.

Iacono, M. J., Delamere, J. S., Mlawer, E. J., Shephard, M. W., Clough, S. A., and Collins, W. D.: Radiative forcing by long-lived greenhouse gases: Calculations with the AER radiative transfer models, J. Geophys. Res., 113, 2008JD009944, https://doi.org/10.1029/2008JD009944, 2008.

Jiménez, P. A., Dudhia, J., González-Rouco, J. F., Navarro, J., Montávez, J. P., and García-Bustamante, E.: A Revised Scheme for the WRF Surface Layer Formulation, Monthly Weather Review, 140, 898–918, https://doi.org/10.1175/MWR-D-11-00056.1, 2012.

Jones, S. C., Harr, P. A., Abraham, J., Bosart, L. F., Bowyer, P. J., Evans, J. L., Hanley, D. E., Hanstrum, B. N., Hart, R. E., Lalaurette, F., Sinclair, M. R., Smith, R. K., and Thorncroft, C.: The Extratropical Transition of Tropical Cyclones: Forecast Challenges, Current Understanding, and Future Directions, Wea. Forecasting, 18, 1052–1092, https://doi.org/10.1175/1520-0434(2003)018%3C1052:TETOTC%3E2.0.CO;2, 2003.

© Author(s) 2026. CC BY 4.0 License.

Kieu, C. Q. and Zhang, D.-L.: A Piecewise Potential Vorticity Inversion Algorithm and Its Application to Hurricane Inner-Core Anomalies, Journal of the Atmospheric Sciences, 67, 2616–2631, https://doi.org/10.1175/2010JAS3421.1, 2010.

Knapp, K. R., Kruk, M. C., Levinson, D. H., Diamond, H. J., and Neumann, C. J.: The International Best Track Archive for Climate Stewardship (IBTrACS), B. Am. Meteorol. Soc., 91, 363–376, doi:10.1175/2009BAMS2755.1, 2010

Liu, Y., Zhang, D.-L., and Yau, M. K.: A Multiscale Numerical Study of Hurricane Andrew (1992). Part I: Explicit Simulation and Verification, Mon. Wea. Rev., 125, 3073–3093, https://doi.org/10.1175/1520-0493(1997)125%3C3073:AMNSOH%3E2.0.CO;2, 1997.

Martinez, J., Bell, M. M., Rogers, R. F., and Doyle, J. D.: Axisymmetric Potential Vorticity Evolution of Hurricane Patricia (2015), Journal of the Atmospheric Sciences, 76, 2043–2063, https://doi.org/10.1175/JAS-D-18-0373.1, 2019.

Mogensen, K. S., Magnusson, L., and Bidlot, J.: Tropical cyclone sensitivity to ocean coupling in the E CMWF coupled model, JGR Oceans, 122, 4392–4412, https://doi.org/10.1002/2017JC012753, 2017.

Molinari, J., Skubis, S., Vollaro, D., Alsheimer, F., and Willoughby, H. E.: Potential Vorticity Analysis of Tropical Cyclone Intensification, J. Atmos. Sci., 55, 2632–2644, https://doi.org/10.1175/1520-0469(1998)055%3C2632:PVAOTC%3E2.0.CO;2, 1998.

Montgomery, M. T., Nicholls, M. E., Cram, T. A., and Saunders, A. B.: A Vortical Hot Tower Route to Tropical Cyclogenesis, Journal of the Atmospheric Sciences, 63, 355–386, https://doi.org/10.1175/JAS3604.1, 2006.

Montgomery, M. T. and Smith, R. K.: Paradigms for tropical cyclone intensification, Aust. Meteorol. Ocean., 64, 37–66, 2014.

https://doi.org/10.5194/egusphere-2026-4860
Preprint. Discussion started: 20 August 2026
© Author(s) 2026. CC BY 4.0 License.

Murthy, V. S. and Boos, W. R.: Understanding the vertical structure of potential vorticity in tropical depressions, Quart J Royal Meteoro Soc, 145, 1968–1991, https://doi.org/10.1002/qj.3539, 2019.

Nguyen, M. C., Reeder, M. J., Davidson, N. E., Smith, R. K., and Montgomery, M. T.: Inner-core vacillation cycles during the intensification of Hurricane *Katrina*, Quart J Royal Meteoro Soc, 137, 829–844, https://doi.org/10.1002/qj.823, 2011.

Röbcke, M., Jones, S. C., and Majewski, D.: The extratropical transition of Hurricane Erin (2001): a potential vorticity perspective, metz, 13, 511–525, https://doi.org/10.1127/0941-2948/2004/0013-0511, 2004.

Rossby, C.-G. and collaborators: Isentropic analysis, B. Am. Meteorol. Soc., 18, 201–209, https://doi.org/10.1175/1520-0477-18.6-7.201, 1937.

Shapiro, L. J. and Möller, J. D.: Influence of Atmospheric Asymmetries on the Intensification of Hurricane Opal: Piecewise PV Inversion Diagnosis of a GFDL Model Forecast, Monthly Weather Review, 131, 1637–1649, https://doi.org/10.1175//2552.1, 2003.

Shi, D. and Chen, G.: Double warm-core structure and potential vorticity diagnosis during the rapid intensification of Supertyphoon Lekima (2019), Journal of the Atmospheric Sciences, https://doi.org/10.1175/JAS-D-20-0383.1, 2021.

Skamarock, W. C., Klemp, J. B., Dudhia, J., Gill, D. O., Liu, Z., Berner, J., Wang, W., Powers, J. G., Duda, M. G., Barker, D. M., and Huang, X.-Y.: A Description of the Advanced Research WRF Model Version 4, NSF National Center for Atmospheric Research, https://doi.org/10.5065/1DFH-6P97, 2019.

Tewari, M., F. Chen, W. Wang, J. Dudhia, M. A. LeMone, K. Mitchell, M. Ek, G. Gayno, J. Wegiel, and R. H. Cuenca, 2004: Implementation and verification of the unified NOAH land surface model in the WRF model. 20th conference on weather analysis and forecasting/16th conference on numerical weather prediction, pp. 11–15.

https://doi.org/10.5194/egusphere-2026-4860
Preprint. Discussion started: 20 August 2026
© Author(s) 2026. CC BY 4.0 License.

Tory, K. J., Montgomery, M. T., Davidson, N. E., and Kepert, J. D.: Prediction and Diagnosis of Tropical Cyclone Formation in an NWP System. Part II: A Diagnosis of Tropical Cyclone Chris Formation, J. Atmos. Sci., 63, 3091–3113, https://doi.org/10.1175/JAS3765.1, 2006.

Yau, M. K., Liu, Y., Zhang, D.-L., and Chen, Y.: A Multiscale Numerical Study of Hurricane Andrew (1992). Part VI: Small-Scale Inner-Core Structures and Wind Streaks, Mon. Wea. Rev., 132, 1410–1433, https://doi.org/10.1175/1520-0493(2004)132%3C1410:AMNSOH%3E2.0.CO;2, 2004.

Wernli, H. and Gray, S. L.: The importance of diabatic processes for the dynamics of synoptic-scale extratropical weather systems – a review, Weather Clim. Dynam., 5, 1299–1408, https://doi.org/10.5194/wcd-5-1299-2024, 2024.

Wu, L. and Wang, B.: A Potential Vorticity Tendency Diagnostic Approach for Tropical Cyclone Motion, Mon. Wea. Rev., 128, 1899–1911, https://doi.org/10.1175/1520- 0493(2000)128%3C1899:APVTDA%3E2.0.CO;2, 2000.

Zhang, D.-L., Liu, Y., and Yau, M. K.: A Multiscale Numerical Study of Hurricane Andrew (1992). Part V: Inner-Core Thermodynamics, Mon. Wea. Rev., 130, 2745–2763, https://doi.org/10.1175/1520-0493(2002)130%3C2745:AMNSOH%3E2.0.CO;2, 2002.

Zhang, D. and Kieu, C. Q.: Shear-forced vertical circulations in tropical cyclones, Geophysical Research Letters, 32, 2005GL023146, https://doi.org/10.1029/2005GL023146, 2005.

Zhang, C. and Wang, Y.: Projected Future Changes of Tropical Cyclone Activity over the Western North and South Pacific in a 20-km-Mesh Regional Climate Model, Journal of Climate, 30, 5923–5941, https://doi.org/10.1175/JCLI-D-16-0597.1, 2017.